J. Fluid Mech. (1990), *vol.* 220, *pp.* 125–160
Printed in Great Britain

The hydrodynamic stability of boundary-layer flow over a class of anisotropic compliant walls

By K. S. YEO

Department of Mechanical and Production Engineering, National University of Singapore, Kent Ridge, Singapore 0511, Republic of Singapore

(Received 9 November 1988 and in revised form 15 March 1990)

This paper examines the linear stability of zero-pressure-gradient boundary-layer flow over a class of anisotropically responding compliant walls. The anisotropic wall behaviour is derived from a material anisotropy which is characterized by relatively high tensile and compressive strength along a certain direction, termed the fibre axis. When the material stiffness along the fibre axis is sufficiently high, the resulting correlation between the horizontal and the vertical components of wall displacement induces at the flow–wall interface a Reynolds shear stress of a sign that is predetermined by the angle with which the fibre axis makes with the direction of the flow. The notion that anisotropic surface response could be employed to produce turbulent Reynolds shear stresses of predetermined sign at a surface was first explored by Grosskreutz (1971) in an experimental study on turbulent drag reduction. The present paper examines the implications of this interesting idea in the context of two-dimensional flow stability over anisotropic compliant walls. The study covers single- and two-layer compliant walls using the methodology described in Yeo (1988). The effects of wall anisotropy, as determined by the orientation of the fibre axis and the material stiffness along the fibre axis, on flow stability are examined for a variety of walls. The potential of some anisotropic compliant walls for delaying laminar–turbulent transition is investigated, and the contribution of the anisotropy to transition delay is appraised.

1. Introduction

Back in the early seventies, Grosskreutz (1971, 1975) proposed and experimented with a novel way of reducing the turbulent shear drag acting on a flat surface subjected to a two-dimensional turbulent shear flow. Grosskreutz's idea was to design an anisotropically responding compliant surface which, when subjected to fluctuating flow stresses, moved in such a manner as to induce a negative Reynolds shear stress at the surface. To achieve the desired result, the typical compliant wall used by Grosskreutz (1971) consisted of a compliant layer supported on an array of regularly spaced stubs which were inclined at 45° into the flow; see figure 1(*a*). The constraining influence arising from the greater stiffness of the wall along the direction of the stubs could then be expected to induce a positive correlation between the horizontal and the vertical components of fluctuating velocity, resulting in the generation of negative Reynolds shear stress in the vicinity of the wall.

Good as the idea may seem, the experimental results obtained by Grosskreutz were, however, less than certain. Modest reduction in drag of up to 5%, computed based on the momentum thickness of the boundary layer, was noted; but more

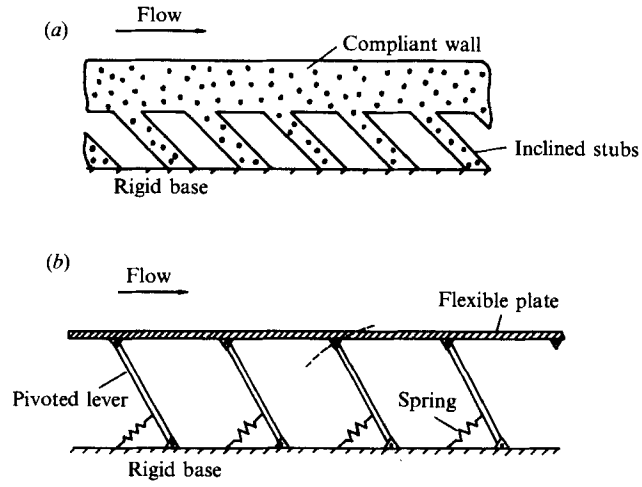

FIGURE 1. Schematic views of (*a*) the inclined-stub wall of Grosskreutz (1971) and (*b*) the sprung-lever flexible-plate wall of Carpenter & Morris (1985).

importantly the walls appeared to perform almost as well when the direction of the inclined stubs was reversed. It is not our purpose here to delve into the probable causes for the rather uncertain results obtained by Grosskreutz, but it is nevertheless pertinent to note that the magnitude and the lengthscale of the velocity fluctuations were likely to be quite small in the vicinity of the surface and might well have failed to elicit sufficient anisotropic response from the wall to produce a significant negative or positive Reynolds shear stress. The resulting influence on the mean flow might hence also have been small, which therefore explains the indifference of the results to a reversal of stub orientation.

There are substantial differences between the dynamics of a turbulent shear flow and that of a linearly unstable laminar shear flow. Therefore, despite the uncertain outcome of Grosskreutz's experiments, the premise of his idea remains theoretically appealing from the point of view of flow stability. As in the case of turbulent shear flows, a negative Reynolds stress would, in a positive mean-velocity gradient, act to transfer energy from the disturbance to the mean flow. This may be expected to have a beneficial influence on the stability of flows over such surfaces. The notion that anisotropic surface response may have a bearing on flow stability is not new, however. Benjamin (1964) made a passing mention of brush-like surfaces in his survey article on flow stability over flexible surfaces. Kramer (1965) also pointed out that the underlying structure of the dolphin skin is anisotropic and suggested that the anisotropy might have contributed in some unknown manner to the flow stabilization which he hypothesized to have taken place over a dolphin in rapid swimming. It was only recently, however, that interest in the flow stabilization potential of anisotropic walls took on a more concrete form. The linear stability of boundary-layer flow over Grosskreutz-type compliant walls was recently explored by Carpenter (1984, 1987) and Carpenter & Morris (1985, 1990). They modelled the anisotropic wall as a thin bending plate supported above a rigid base by a continuous array of inclined rigid sprung levers; see figure 1 (*b*). Because of the assumed rigidity of the levers, the displacement of the surface could only take place along directions perpendicular to the axis of the levers. This constrained motion of the surface produced, via the non-slip condition, a fixed correlation between the horizontal and

the vertical components of disturbance flow velocity, resulting therefore in the induction of Reynolds shear stress of fixed predetermined sign in the vicinity of the wall. The Carpenter–Morris model hence does correctly capture the essence of Grosskreutz's idea. As a model of Grosskreutz's actual walls, however, it is slightly deficient in that the levers are rigid whereas the silicon-rubber stubs may stretch and compress along their axis. Their results indicate that the Grosskreutz-type walls may be capable of achieving significant delay of transition to turbulence. A summary of the work they have done up till very recently is given in Carpenter & Morris (1990).

In this paper we present a different model of Grosskreutz's walls. This is a homogeneous continuum material model. Anisotropic surface response similar to that of Grosskreutz's walls is obtained by adopting a material anisotropy which allows for strong resistance to extension/compression to be specified along a given direction, termed the fibre axis. The simplest common model of anisotropy which can meet this requirement is transverse isotropy. A transversely isotropic material is characterized by the existence of an axis, termed the axis of isotropy, about which the properties of the material are identical in all directions perpendicular to this axis. To have a better physical appreciation of the nature of the anisotropy, it is useful to note that this kind of material anisotropy is quite commonly associated with composite materials which are derived from the reinforcement of a soft isotropic material (the matrix) by a parallel family of straight fibres of a stiffer material, see figure 2; the axis of the fibres (fibre axis) is then the axis of isotropy. If the reinforcing fibres are very stiff, extension/compression of the material along the direction of the fibres will be strongly resisted by the fibres. As a model for the Grosskreutz walls, the present model has an advantage over the rigid-lever model of Carpenter & Morris in that it also allows for surface displacement to occur along the fibre axis when the material is specified to have finite stiffness along the axis. However, the present model is not intended and cannot claim to be a precise replica of Grosskreutz's inclined-stub walls, which are non-continuum to begin with.

The two-dimensional stability of zero-pressure-gradient boundary layers over single- and multi-layer isotropic-material compliant walls had been studied by Yeo (1988). In this paper, we are interested in the effects of Grosskreutz-type anisotropic surface behaviour on the stability of the same flow. Section 2 sets out the essential theory, beginning with a description of the transverse-isotropy-material model and then its stress–strain constitutive law. The formulation of the stability eigenvalue problem for the coupled system of flow and wall follows the basic methodology (and terminology) described in Yeo (1988). The theory developed is more generally applicable to material anisotropies which possess a plane of symmetry parallel to the (x_1, x_3)-plane of the stability problem. The latter condition is a weak symmetry requirement imposed to ensure that two-dimensional wall modes which are compatible with the Orr–Sommerfeld disturbance modes of the flow exist. The present paper can be regarded as a sequel to Yeo (1988), which is referred to hereinafter as I. Results showing the effects of the anisotropy on flow stability over single- and two-layer transversely isotropic material walls are presented and discussed in §3. To keep the anisotropic surface response simple, the two-layer cases examined are limited to walls which comprise a thin layer of stiff isotropic material bonded onto a much thicker but softer layer of transversely isotropic material.

While the study is restricted to two-dimensional disturbance normal modes, it is important to note that three-dimensional modes can become important in walls which are highly compliant. Nevertheless, two-dimensional studies do provide a good and relatively cheaper preliminary assessment of the stabilization potential of

compliant walls in general. The study of three-dimensional modes is outside the scope of the present paper. Unlike the case of isotropic-material walls, the three-dimensional eigenvalue problem for flow over anisotropic-material walls does not, in general, admit reduction to an equivalent two-dimensional one. A study of the three-dimensional eigenvalue problem for flow over anisotropic-material walls is presented in Yeo (1986).

2. Theory

Figure 2(*a*) shows schematically a two-dimensional boundary layer over a compliant wall which is composed of a uniformly thick layer of transversely isotropic material backed by a rigid base. The coordinate frame for the stability problem (x_1, x_2, x_3) has its positive x_1-axis pointing in the streamwise direction from left to right. The unperturbed surface of the compliant wall spans the (x_1, x_2)-plane. $(x_1^{(m)}, x_2^{(m)}, x_3^{(m)})$ denotes the material-property coordinate frame, with respect to which the material properties of the layer will be specified.

2.1. *Homogeneous transverse isotropy*

2.1.1. *An introduction to transversely isotropic materials*

Transverse isotropy is one of the simplest forms of material anisotropy. It represents in the hierarchy of material anisotropy the next level of complexity to isotropy. For an isotropic material, the mechanical properties are identical in all directions. In the case of a transversely isotropic material, there is a distinguished direction, termed the *axis of isotropy*. This choice of term is used to indicate that the material properties of a transversely isotropic material are identical with respect to all directions perpendicular to the distinguished direction. Planes normal to the axis of isotropy are consequently *planes of isotropy*. Transverse isotropy literally means isotropy in the planes transverse to the axis.

In practice, transversely isotropic material behaviour is most commonly realized in fibre-reinforced composite materials which are derived by embedding a parallel family of straight fibres in an isotropic matrix, see figure 2(*b*). Figure 2(*b*) shows a fibre-reinforced material with straight fibres aligned with the $x_3^{(m)}$-axis of the material-property coordinate frame. If the fibres are arranged randomly or in accordance with the hexagonal symmetry shown in figure 2(*b*) on a plane normal to the fibres, then the mechanical properties of the material will be the same for all directions lying in the plane; that is, isotropic with respect to all directions perpendicular to the parallel fibres. In making this statement, we have implicitly assumed that the physical processes that are envisaged occur on a lengthscale that is significantly longer than the average spacing between adjacent fibres, so that the discrete nature of the fibres does not matter and the material behaves as if it were homogeneous. The direction along which the fibres lie, the $x_3^{(m)}$-axis, is then clearly the axis of isotropy and is also called the *fibre axis* for short in this paper. Planes parallel to the $(x_1^{(m)}, x_2^{(m)})$-plane are then planes of isotropy.

For such composites, it is usual for the fibres to be produced from a material that is much stiffer than the embedding isotropic matrix. The stretching and compression of the material is then more strongly resisted along the fibre axis than in any other directions. If such a composite material is employed for a compliant layer, as is shown in figure 2(*a*) (with its fibre axis in the (x_1, x_3)-plane), and if further the fibres are very stiff, then the displacement of the surface of the wall along the fibre axis will be

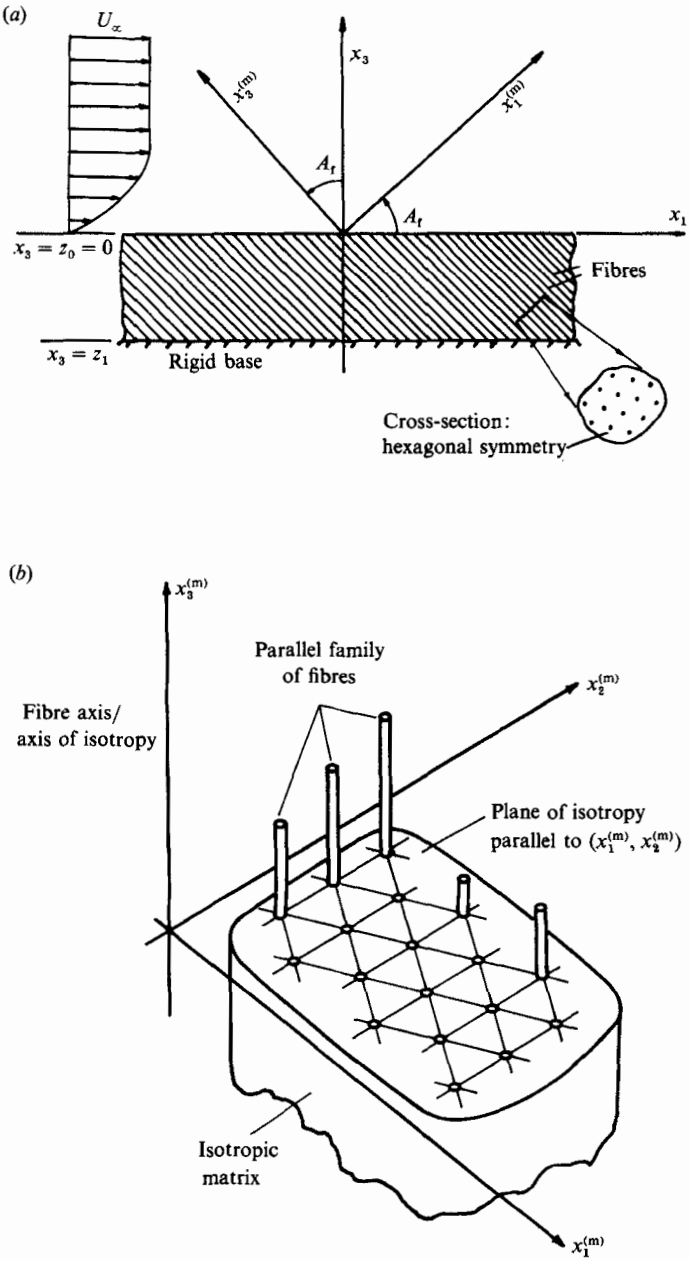

FIGURE 2. (*a*) Schematic view of flow over a uniformly thick layer of transversely isotropic (fibre-reinforced-type) material. (x_1, x_2, x_3) is the coordinate frame for the stability problem. $(x_1^{(m)}, x_2^{(m)}, x_3^{(m)})$ is the material-property coordinate frame. (*b*) $(x_1^{(m)}, x_2^{(m)})$-section of a fibre-reinforced specimen with some protruding fibres shown. Isotropy in the $(x_1^{(m)}, x_2^{(m)})$-plane is achieved by arranging the parallel fibres hexagonally as shown or randomly.

strongly resisted. This will result in an anisotropic response which is very similar to that of the Grosskreutz walls and the theoretical model of Carpenter & Morris; figure 1 (*a*, *b*). It is important to note, however, that fibre-reinforced composites are not the only types of material that may exhibit transverse isotropy. We have made frequent references to these composites only because these may help to give readers who

are not familiar with the subject of material anisotropy a physical feel for the nature of the anisotropy studied here. The physical interpretation in terms of fibre-reinforced composites is useful, but not necessary, for the purposes here. And we do not intend to pursue further the finer points which relate to the actual physical realization of our wall model. There are other materials which may exhibit transverse isotropy: materials with appropriate distributions of voids are examples; the naturally evolved skin layer of dolphins, see figure 2 of Carpenter & Garrad (1985), may possibly be transversely isotropic too.

2.1.2. *Constitutive relation for transversely isotropic materials*

The stress–strain constitutive relation for a general anisotropic material, with viscous-type damping, undergoing small-amplitude sinusoidal deformation may be given in the form

$$\sigma_{pq}^{(\mathrm{m})} = C_{pqrs}^{(\mathrm{m})} \epsilon_{rs}^{(\mathrm{m})}, \tag{1}$$

where $[\sigma_{pq}]$ and $[\epsilon_{rs}]$ are respectively the stress and the strain tensors. $[C_{pqrs}]$ is called the viscoelastic modulus tensor here and its components are in general complex and functions of frequency ω. The superscript (m) denotes that the tensors are specified with respect to the material-property frame. The material-property frame is usually chosen such that the modulus tensor $[C_{pqrs}]$ assumes its simplest form, with the maximum number of zeros. The strain tensor field is defined in terms of the displacement field $\boldsymbol{\eta} = (\eta_1, \eta_2, \eta_3)^{\mathrm{T}}$ by

$$\epsilon_{rs} = \tfrac{1}{2}(\eta_{r,s} + \eta_{s,r}). \tag{2}$$

Einstein's convention on repeated indices and subscript commas is assumed throughout this paper.

The viscoelastic modulus tensor $[C_{pqrs}]$ satisfies the following symmetry conditions:

$$C_{pqrs} = C_{qprs} = C_{pqsr} \quad \text{and} \quad C_{pqrs} = C_{rspq}. \tag{3}$$

These conditions reduce the number of independent components of $[C_{pqrs}]$ to a maximum of 21 for the most general homogeneous anisotropic medium. The number is reduced to 13 if the material exhibits a plane of symmetry perpendicular to which the properties are identical. A material exhibiting two or three mutually orthogonal planes of symmetry is termed *orthotropic*. An orthotropic material has a maximum of nine independent moduli. A transversely isotropic material, the anisotropy of interest here, is characterized by the existence of an axis of isotropy; the properties are identical in all directions perpendicular to this axis. In fact, identity in six evenly spaced (60°) directions about the axis is sufficient for transverse isotropy (see p. 24 of Lekhnitskii 1963); which is also why the fibres in figure 2(*a*, *b*) are shown to be arranged according to hexagonal symmetry. A transversely isotropic material has a maximum of five independent moduli in $[C_{pqrs}]$. Useful references on the subject of material anisotropy include Landau & Lifshitz (1970) and Green & Zerna (1968). The former contains a short section on viscous dissipation in anisotropic materials.

The stress–strain relation for the most general transversely isotropic material, with the axis of isotropy specified along the $x_3^{(\mathrm{m})}$-axis, can be represented in the form

$$\Sigma^{(\mathrm{m})} = \boldsymbol{C}^{(\mathrm{m})} \mathscr{E}^{(m)} \tag{4a}$$

where

$$\mathscr{E}^{(\mathrm{m})} = (\epsilon_{11}, \epsilon_{22}, \epsilon_{33}, 2\epsilon_{23}, 2\epsilon_{13}, 2\epsilon_{12})^{\mathrm{T(m)}}, \quad \Sigma^{(\mathrm{m})} = (\sigma_{11}, \sigma_{22}, \sigma_{33}, \sigma_{23}, \sigma_{13}, \sigma_{12})^{\mathrm{T(m)}}$$

and $\boldsymbol{C}^{(\mathrm{m})}$ is a matrix, commonly called the stiffness matrix, given by

$$\boldsymbol{C}^{(\mathrm{m})} = \begin{bmatrix} C_{1111} & C_{1122} & C_{1133} & 0 & 0 & 0 \\ C_{1122} & C_{1111} & C_{1133} & 0 & 0 & 0 \\ C_{1133} & C_{1133} & C_{3333} & 0 & 0 & 0 \\ 0 & 0 & 0 & C_{1313} & 0 & 0 \\ 0 & 0 & 0 & 0 & C_{1313} & 0 \\ 0 & 0 & 0 & 0 & 0 & \frac{1}{2}(C_{1111}-C_{1122}) \end{bmatrix}^{(\mathrm{m})}, \tag{4b}$$

see Green & Zerna (1968). The components of $\boldsymbol{C}^{(\mathrm{m})}$ are in terms of the components from the viscoelastic modulus tensor $[C_{pqrs}]^{(\mathrm{m})}$. The five independent components in (4*b*) can be expressed in terms of five physically meaningful and experimentally measurable quantities; shear moduli G and G', Poisson's ratios ν and ν', and Young's modulus E':

$$C^{(\mathrm{m})}_{1111} = G+M^{-1}, \quad C^{(\mathrm{m})}_{1122} = -G+M^{-1}, \quad C^{(\mathrm{m})}_{1133} = 2\nu' M^{-1} \tag{5a, b, c}$$

$$C^{(\mathrm{m})}_{1313} = G', \quad C^{(\mathrm{m})}_{3333} = E'+4\nu'^2 M^{-1}, \tag{5d, e}$$

where $M = 2(1-\nu)E^{-1}-4\nu'^2E'^{-1}$, and $E = 2G(1+\nu)$. Equations (5) can be obtained by solving equations (3.14) of Lekhnitskii (1963) for the stress components in terms of strain components (with axis of isotropy along $x_3^{(\mathrm{m})}$) and then identifying the coefficients with the components of $[C^{(\mathrm{m})}_{pqrs}]$ using (4).

The two parameters G and G' govern the behaviour of the material in the shear mode: G denotes the shear modulus for shearing which occurs in planes of isotropy, $\sigma^{(\mathrm{m})}_{12} = 2G\epsilon^{(\mathrm{m})}_{12}$; G' is the shear modulus for shearing which occurs in planes normal to a plane of isotropy, in particular $\sigma^{(\mathrm{m})}_{13} = 2G'\epsilon^{(\mathrm{m})}_{13}$ and $\sigma^{(\mathrm{m})}_{23} = 2G'\epsilon^{(\mathrm{m})}_{23}$. E' is the Young's modulus of the material along the axis of isotropy (or fibre axis). It governs the stiffness of the material in uniaxial extension and compression (only $\sigma^{(\mathrm{m})}_{33} \neq 0$) along $x_3^{(\mathrm{m})}$; $\sigma^{(\mathrm{m})}_{33} = E'\epsilon^{(\mathrm{m})}_{33}$. When E' is large, stretching of the material along the axis of isotropy is strongly resisted. The transverse reduction which occurs in the plane of isotropy owing to uniaxial extension along the axis of isotropy is denoted by the Poisson's ratio ν'; $\epsilon^{(\mathrm{m})}_{11} = -\nu'\epsilon^{(\mathrm{m})}_{33}$. ν denotes the Poisson's ratio characterizing transverse reduction in the plane of isotropy for uniaxial extension along a direction lying in the plane of isotropy.

When specifying the properties of transversely isotropic materials, it is much more intelligible to talk and think in terms of these experimentally measurable material parameters than the raw components of $[C_{pqrs}]^{(\mathrm{m})}$. Once G, G', E', ν and ν' are known, the non-zero components of $[C_{pqrs}]^{(\mathrm{m})}$ are completely determined via (5). It is useful to note that a transversely isotropic material becomes isotropic when $G = G'$, $\nu = \nu'$ and $E' = E = 2G(1+\nu)$. An isotropic material is characterized by just two independent moduli.

Figure 2(*a*) shows the relationship between the material-property coordinate frame and the coordinate frame for the stability problem. A_{f} is the angle in degrees with which the axis $x_3^{(\mathrm{m})}$ is rotated from the x_3-axis, measured positively in the anticlockwise direction. When posing the stability problem in the (x_1, x_2, x_3)-frame we need to know the stress–strain law of the material of the layer in this frame. The moduli tensor $[C_{ijkl}]$ in the frame of the stability problem can be obtained from $[C_{pqrs}]^{(\mathrm{m})}$ by applying the transformation rule for Cartesian tensors,

$$C_{pqrs} = C^{(\mathrm{m})}_{ijkl}\, l_{pi}\, l_{qj}\, l_{rk}\, l_{sl} \tag{6}$$

where the non-zero direction cosines are $l_{11} = \cos A_f$, $l_{13} = -\sin A_f$, $l_{31} = -l_{13}$ and $l_{33} = l_{11}$.

2.2. *Stability of the flow–wall system*

We now consider the stability of the coupled system of flow and anisotropic wall to small-amplitude sinusoidal disturbances having the variation $e^{i\alpha x_1}e^{-i\omega t}$. This represents an x_1-travelling wave with phase speed $c = \omega/\alpha$ where ω and α are respectively the frequency and the x_1-wavenumber of the disturbance wave.

2.2.1. *Flow stability equation*

The basic flow of interest here is the zero-pressure-gradient boundary-layer flow over a flat surface. We assume the flow to be locally parallel and given by the Blasius solution to Prandtl's boundary-layer equations. In dimensionless form, the x_1-component of the basic flow is given by

$$U(x_3) = f'(x_3), \tag{7a}$$

where $f(x_3)$, the Blasius stream function, satisfies the equation

$$2f''' + m^2 f'' f = 0 \tag{7b}$$

subject to the boundary conditions $f(0) = f'(0) = 0$ and $f'(\infty) = 1$. The prime denotes an ordinary derivative with respect to x_3. All quantities relevant to the flow domain are assumed to have been non-dimensionalized with respect to the following reference scales: $U_\infty^{(d)}$ (free-stream velocity) for velocities, $\delta^{(d)}$ ($= m(\nu_f^{(d)} x_1^{(d)}/U_\infty^{(d)})^{\frac{1}{2}}$) for lengths and $\rho_f^{(d)}$ (fluid density) for density. Here $\nu_f^{(d)}$ is the kinematic viscosity and $x_1^{(d)}$ is the distance from the leading edge. Superscript (d) indicates that the marked quantity is dimensional. We take $\delta^{(d)}$ to be the local displacement thickness, in which case $m = 1.72078$. The approximation of the basic flow by the Blasius profile $U(x_3)$ and the assumption of local flow parallelism are valid when the streamwise Reynolds number R_x ($= U_\infty^{(d)} x_1^{(d)}/\nu_f^{(d)}$) is large.

The stability analysis simplifies tremendously when the flow is assumed to be locally parallel. Let $\epsilon \boldsymbol{u} = (\epsilon u_1, 0, \epsilon u_3)^T$ be a two-dimensional perturbation of the locally parallel basic flow $U(x_3)\boldsymbol{i}_1$ and $\epsilon\Phi$ the corresponding perturbation stream function (ϵ is a small real quantity) so that $u_1 = \Phi_{,3}$ and $u_3 = -\Phi_{,1}$; then in the normal-mode analysis, Φ has a separable solution of the form $\phi(x_3)e^{i\alpha x_1}e^{-i\omega t}$, where the x_3-dependent function $\phi(x_3)$ is governed by the Orr–Sommerfeld equation

$$(U-c)(\phi'' - \alpha^2\phi) - U''\phi = \frac{1}{i\alpha R_\delta}(\phi'''' - 2\alpha^2\phi'' + \alpha^4\phi). \tag{8}$$

$R_\delta = U_\infty^{(d)}\delta^{(d)}/\nu_f^{(d)}$ denotes the Reynolds number based on the local displacement thickness $\delta^{(d)}$.

2.2.2. *Wave propagation in anisotropic-material walls*

We next consider the dynamics of wave propagation in a compliant wall which may be composed of one or more uniformly thick layers of transversely isotropic materials. The treatment given below is, however, also applicable to homogeneous materials of more general anisotropy. No significant simplification is obtained by restricting the analysis only to transversely isotropic materials because the moduli tensor $[C_{ijkl}]$ in the coordinate frame (x_1, x_2, x_3), derived by transformation from $[C_{pqrs}]^{(m)}$, can be quite complex (containing many non-zero terms).

The non-dimensionalization of all quantities relevant to the wall follows that of the flow with the exception of the lengthscale. A fixed lengthscale, denoted by $L_{\mathrm{w}}^{(\mathrm{d})}$, rather than the local boundary-layer lengthscale $\delta^{(\mathrm{d})}$ is used. This is because the latter varies with the downstream distance whereas the parameters of the compliant layers do not. A fixed reference lengthscale with respect to which the wall parameters remain constant is to be preferred. The wall lengthscale $L_{\mathrm{w}}^{(\mathrm{d})}$ is defined implicitly through the specification of a reference Reynolds number denoted by

$$R_{\mathrm{w}} = U_{\infty}^{(\mathrm{d})} L_{\mathrm{w}}^{(\mathrm{d})} / \nu_{\mathrm{f}}^{(\mathrm{d})}.$$

Let us consider the propagation of small-amplitude disturbances in a single homogeneous anisotropic layer. The displacement field of the disturbance $\boldsymbol{\eta} = (\eta_1, \eta_2, \eta_3)^{\mathrm{T}}$ is governed by the momentum equations

$$\rho \ddot{\eta}_p = \sigma_{pq,q} \quad (p = 1, 2, 3), \tag{9a}$$

with

$$\sigma_{pq} = C_{pqrs}\, \epsilon_{rs}, \tag{9b}$$

and ϵ_{rs} being as defined in (2); see Section 34 of Landau & Lifshitz (1970). Each dot above η_p signifies partial derivative with respect to time t. Equations (9) admit x_1-propagating wave solutions of the form

$$\eta_p = \hat{\eta}_p(x_3)\, \mathrm{e}^{\mathrm{i}\alpha x_1}\, \mathrm{e}^{-\mathrm{i}\omega t} \quad (p = 1, 2, 3) \tag{10a}$$

where $\hat{\eta}_p$, the x_3-dependent amplitude, has the form

$$\hat{\eta}_p = B_p\, \mathrm{e}^{\mathrm{i}\gamma x_3} \quad (B_p \text{ is a complex constant}). \tag{10b}$$

The substitution of (10a, b) into (9) yields a set of homogeneous linear equations in B_s:

$$(\rho\omega^2 \delta_{ps} - C_{pqrs}\, k_q\, k_r) B_s = 0 \quad (p = 1, 2, 3), \tag{11}$$

where $(k_1, k_2, k_3) = (\alpha, 0, \gamma)$. δ_{ps} is the Kronecker delta. The existence of a non-trivial solution vector $\boldsymbol{B} = (B_1, B_2, B_3)^{\mathrm{T}}$ is then given by the condition that the determinant of (11) is zero. For a wave of specified α and ω, the determinantal equation is a six-degree polynomial equation in γ. Assuming the six γ-roots to be distinct for simplicity, there are then six fundamental solutions of the form of (10) from which all x_1-propagating waves of given α and ω are linearly constituted. In the most general case, some or all of the six eigenvectors $\boldsymbol{B}$ associated with the γ-roots may be non-zero in all its components; $B_j \neq 0$ for $j = 1, 2, 3$. These correspond to x_1-travelling waves with a three-dimensional displacement field. These three-dimensional modes are not compatible with the two-dimensional disturbance modes $(u_1, 0, u_3)^{\mathrm{T}}$ of the flow because the non-zero η_2 component of wall displacement would excite a u_2 component in the flow hence rendering the stability problem effectively three-dimensional. Such modes are outside the scope of the present paper. A theoretical treatment applicable to this more general case is given in Yeo (1986).

Such x_1-propagating three-dimensional fundamental wall modes ($B_j \neq 0$ for $j = 1, 2, 3$), however, do not exist for the class of walls investigated here. In fact, such three-dimensional modes do not exist whenever the material properties of the wall are symmetric about the (x_1, x_3)-plane. The (x_1, x_3)-plane is clearly a plane of symmetry for the cases of interest here because it contains the axis of isotropy $x_3^{(\mathrm{m})}$, figure 2(a). The existence of a plane of symmetry is a very weak symmetry condition. The analysis given below is therefore applicable to a very large class of anisotropic materials.

When the material properties are symmetric about the (x_1, x_3)-plane, all the components of the moduli tensor $[C_{pqrs}]$ which contain the index 2 either one or three times must be zero; see §5.4 of Green & Zerna (1968). Equations (11) then simplify to

$$(C_{1111}\alpha^2 + C_{1313}\gamma^2 + 2C_{1113}\alpha\gamma - \rho\omega^2)B_1 + (C_{1113}\alpha^2 + C_{3313}\gamma^2 + (C_{1133} + C_{1313})\alpha\gamma)B_3 = 0, \quad (12a)$$

$$(C_{2112}\alpha^2 + C_{2332}\gamma^2 + 2C_{2132}\alpha\gamma - \rho\omega^2)B_2 = 0, \quad (12b)$$

$$(C_{1113}\alpha^2 + C_{3313}\gamma^2 + (C_{1133} + C_{1313})\alpha\gamma)B_1 + (C_{1313}\alpha^2 + C_{3333}\gamma^2 + 2C_{3313}\alpha\gamma - \rho\omega^2)B_3 = 0. \quad (12c)$$

The determinant of (12) has the factored form

$$(\mathrm{Coef}\, B_2)\,\Delta = 0, \quad (13)$$

where $(\mathrm{Coef}\, B_2)$ is the coefficient of B_2 in (12b) and Δ is the determinant obtained from the coefficients of B_1 and B_3 in (12a, c). $(\mathrm{Coef}\, B_2)$ is quadratic in γ. Two γ-roots are obtained from $(\mathrm{Coef}\, B_2) = 0$ while the remaining four γ-roots come from $\Delta = 0$. It is easy to see, from (12), that the $\boldsymbol{B}$-eigenvectors for the two γ-roots of $(\mathrm{Coef}\, B_2) = 0$ have the form $(0, B_2, 0)^{\mathrm{T}}$. These correspond to a one-dimensional fundamental plane wave with displacement field $(0, \eta_2, 0)^{\mathrm{T}}$ propagating in the x_1-direction. Similarly the four γ-roots of $\Delta = 0$ have $\boldsymbol{B}$-eigenvectors of the form $(B_1, 0, B_3)^{\mathrm{T}}$ which are two-dimensional (plane-strain) fundamental x_1-propagating plane waves.

The two plane-wave solutions in the first group with $\eta_1 = \eta_3 = 0$ are of little interest to us here. Such waves also exist for isotropic material layers. Dynamically these one-dimensional (anti-plane) wave modes are coupled via the non-slip condition $u_2 = \dot{\eta}_2$ at the flow–wall interface to the x_2-component of disturbance flow velocity $u_2 = \hat{u}_2 \mathrm{e}^{\mathrm{i}\alpha(x_1 - ct)}$, which is governed by the following equation

$$\hat{u}_2'' - [\alpha^2 + \mathrm{i}\alpha R_\delta (U - c)]\,\hat{u}_2 = 0; \quad (14)$$

see §5.1 of Yeo (1986). A one-dimensional eigenvalue problem which determines the linear stability of $U(x_3)\boldsymbol{i}_1$ to u_2-perturbations can be formulated; which is distinct from the two-dimensional Orr–Sommerfeld problem. It suffices for the purposes here to note that the eigenvalue spectrum of this one-dimensional stability problem can be shown to comprise only damped (time-asymptotic) modes (Yeo 1990).

The two-dimensional plane-wave solutions associated with the four γ-roots of $\Delta = 0$ are compatible with the OS modes of the flow, and hence are the solutions of interest here. We denote the four γ-roots and their corresponding eigenvectors by

$$\gamma_n \quad \text{and} \quad \boldsymbol{B}^{(n)} = (B_1^{(n)}, 0, B_3^{(n)})^{\mathrm{T}} \quad (n = 1, \ldots, 4),$$

where the superscript (n) denotes the nth root. Assuming the γ-roots to be distinct for simplicity, the four wave solutions

$$\boldsymbol{\eta}^{(n)} = \boldsymbol{B}^{(n)} \mathrm{e}^{\mathrm{i}\gamma_n x_3} \mathrm{e}^{\mathrm{i}\alpha x_1} \mathrm{e}^{-\mathrm{i}\omega t} \quad (n = 1, \ldots, 4) \quad (15)$$

form a fundamental system of solutions for two-dimensional x_1-propagating waves of given α and ω. Any x_1-propagating wave $\boldsymbol{\eta}$ can be represented as a linear combination of the four fundamental solutions as

$$\boldsymbol{\eta} = \sum_{n=1}^{4} D_n \boldsymbol{\eta}^{(n)}, \quad (16)$$

where $D_n (n = 1, \ldots, 4)$ are complex constants determined by the boundary conditions on the layer. There is an established procedure for treating cases with repeated γ-

roots; see Hirsch & Smale (1974). The complex x_3-dependent amplitude functions of the two-dimensional displacement field $\boldsymbol{\eta} = (\eta_1, 0, \eta_3)^{\mathrm{T}}$ are

$$\hat{\eta}_p = \sum_{n=1}^{4} D_n B_p^{(n)} \mathrm{e}^{\mathrm{i}\gamma_n x_3} \quad (p = 1 \quad \text{and} \quad 3). \tag{17}$$

Substituting (16) into the constitutive relation (9*b*) yields

$$\sigma_{pq} = \hat{\sigma}_{pq} \mathrm{e}^{\mathrm{i}\alpha x_1} \mathrm{e}^{-\mathrm{i}\omega t}, \tag{18a}$$

where $$\hat{\sigma}_{pq} = \sum_{n=1}^{4} \mathrm{i} D_n \mathrm{e}^{\mathrm{i}\gamma_n x_3} [(\alpha C_{pq11} + \gamma_n C_{pq13}) B_1^{(n)} + (\alpha C_{pq13} + \gamma_n C_{pq33}) B_3^{(n)}]. \tag{18b}$$

Following I, we define the displacement–stress vector which characterizes the displacement and the stress state for points in the layer as follows:

$$\boldsymbol{S}(x_3) = (\hat{\eta}_1, \hat{\eta}_3, \hat{\sigma}_{31}, \hat{\sigma}_{33})^{\mathrm{T}}.$$

From (17) and (18*b*), $\boldsymbol{S}(x_3)$ is linearly related to the constant vector $\boldsymbol{D} = (D_1, \ldots, D_4)^{\mathrm{T}}$ as follows

$$\boldsymbol{S}(x_3) = \boldsymbol{Q}(x_3) \boldsymbol{D}, \tag{19a}$$

where $\boldsymbol{Q}(x_3)$ is a 4×4 matrix with the components

$$Q_{1n} = B_1^{(n)} E_n, \quad Q_{2n} = B_3^{(n)} E_n, \tag{19b, c}$$

$$Q_{3n} = \mathrm{i}[(\alpha C_{1113} + \gamma_n C_{1313}) B_1^{(n)} + (\alpha C_{1313} + \gamma_n C_{1333}) B_3^{(n)}] E_n, \tag{19d}$$

$$Q_{4n} = \mathrm{i}[(\alpha C_{1133} + \gamma_n C_{1333}) B_1^{(n)} + (\alpha C_{1333} + \gamma_n C_{3333}) B_3^{(n)}] E_n, \tag{19e}$$

and $$E_n = \mathrm{e}^{\mathrm{i}\gamma_n x_3} \quad (n = 1, \ldots, 4).$$

It can be seen from (12*a*, *c*) and (19) that only six moduli really matter as far as two-dimensional wave propagation in the x_1-direction is concerned, although 13 material parameters are needed for the most general anisotropic material with symmetry about the (x_1, x_3)-plane.

For a homogeneous layer of thickness $h\,(= a - b)$, extending from $x_3 = a$ to $x_3 = b$ (lower surface), we have, using equation (19*a*),

$$\boldsymbol{S}(b) = \boldsymbol{P}(b, a) \boldsymbol{S}(a) \tag{20}$$

where $\boldsymbol{P}(b, a) = \boldsymbol{Q}(b) [\boldsymbol{Q}(a)]^{-1}$ is termed the propagation matrix. $\boldsymbol{P}(b, a)$ relates the displacement–stress state at the top of the layer to that at the bottom. The important properties of $\boldsymbol{P}(b, a)$ are given in I.

The use of the propagation matrix permits a systematic treatment of wave propagation in compliant walls comprising any finite number of uniformly thick layers. For a compliant wall comprising n layers of anisotropic materials (with properties symmetric about the (x_1, x_3)-plane), let $\boldsymbol{P}^{(j)}(z_j, z_{j-1})$ denote the propagation matrix of the jth layer, which is located between $x_3 = z_{j-1}$ and $x_3 = z_j$ (lower surface). Assuming that adjacent layers are bonded together so that displacement and stress are continuous across the interface, we have, using (20) recursively,

$$\boldsymbol{S}(z_n) = \boldsymbol{P}^{(n)}(z_n, z_{n-1}) \boldsymbol{S}(z_{n-1}) = \boldsymbol{P}^{\mathrm{O}} \boldsymbol{S}(z_0), \tag{21}$$

where $$\boldsymbol{P}^{\mathrm{O}} = \prod_{j=n}^{1} \boldsymbol{P}^{(j)}(z_j, z_{j-1})$$

is termed the overall propagation matrix for the compliant wall. $\boldsymbol{P}^{\mathrm{O}}$ linearly relates the displacement–stress state at the top surface of the wall at $x_3 = z_0$ to that at the bottom of the last compliant layer at $x_3 = z_n$. More details are available in I.

2.2.3. *Fluid–wall coupling and the stability eigenvalue problem*

Having established the necessary dynamics governing the two-dimensional disturbances in the flow and the wall, it remains to relate these at the flow–wall interface to complete the formulation of the eigenvalue problem. The interaction of the two media at their interface is governed by the condition of velocity continuity. The relevant equations, linearized about the mean interface at $x_3 = z_0$, are

$$\dot{\eta}_1 = u_1 + U'\eta_3, \quad \dot{\eta}_3 = u_3. \tag{22a, b}$$

The linearized disturbance flow stresses acting on the wall are

$$\sigma_{31} = \frac{1}{R_w}\left[\phi'' + \alpha^2\phi + \frac{U''}{c}\phi\right]_{z_0} e^{i\alpha x_1} e^{-i\omega t}, \tag{23a}$$

$$\sigma_{33} = \left[\frac{-1}{i\alpha R_w}\phi''' - \left(c + \frac{3i\alpha}{R_w}\right)\phi' - U'\phi\right]_{z_0} e^{i\alpha x_1} e^{-i\omega t}. \tag{23b}$$

Note that $U''(z_0) = 0$ for the Blasius velocity profile. The non-dimensionalization scheme used in §2.2.2 is applicable to (22) and (23); in particular the lengthscale is $L_w^{(d)}$. These equations, whose detailed derivation is given in I, are valid irrespective of the specific constitutive (stress–strain) relation for the compliant material. The interaction between the flow and the wall as given by (22) and (23) can be recast in the form

$$\boldsymbol{S}(z_0) = \boldsymbol{Q}_c(z_0)\boldsymbol{\phi}^{(w)}(z_0), \tag{24a}$$

where

$$\boldsymbol{Q}_c = \begin{bmatrix} iU'(c\omega)^{-1} & i\omega^{-1} & 0 & 0 \\ c^{-1} & 0 & 0 & 0 \\ (\alpha^2 + U''c^{-1})R_w^{-1} & 0 & R_w^{-1} & 0 \\ -U' & -(c + 3i\alpha R_w^{-1}) & 0 & -(i\alpha R_w)^{-1} \end{bmatrix} \tag{24b}$$

and

$$\boldsymbol{\phi} = (\phi, \phi', \phi'', \phi''')^T.$$

$\boldsymbol{Q}_c$ is called the flow–wall coupling matrix. The superscript (w) is used above for the sole purpose of indicating that the $\boldsymbol{\phi}$ in (24) is to be interpreted in the wall lengthscale of $L_w^{(d)}$ like the other quantities of the equation. From (21) and (24*a*) we have the final form

$$\boldsymbol{S}(z_n) = \boldsymbol{P}^0\boldsymbol{Q}_c\boldsymbol{M}_s\boldsymbol{\phi}(z_0), \tag{25}$$

where $\boldsymbol{M}_s = \mathrm{Diag}\{r, 1, r^{-1}, r^{-2}\}(r = R_\delta/R_w)$. $\boldsymbol{M}_s$ relates the flow disturbance amplitude function $\boldsymbol{\phi}^{(w)}$ in the lengthscale $L_w^{(d)}$ to $\boldsymbol{\phi}$ in the local flow lengthscale $\delta^{(d)}$; $\boldsymbol{\phi}^{(w)} = \boldsymbol{M}_s\boldsymbol{\phi}$. In (25), the matrices $\boldsymbol{P}^0$ and $\boldsymbol{Q}_c$ are in the wall lengthscale while $\boldsymbol{\phi}$ is in the flow lengthscale of $\delta^{(d)}$. More details concerning the scheme of non-dimensionalization are given in §2.4 of I. Equation (25) relates the disturbance in the flow at the mean flow–wall interface $\boldsymbol{\phi}(z_0)$ to the displacement–stress state $\boldsymbol{S}(z_n)$ at the bottom surface of the last (nth) compliant layer. The last layer is assumed for the purposes here to be perfectly bonded onto a flat rigid base; that is $\hat{\eta}_1(z_n) = \hat{\eta}_3(z_n) = 0$.

2.2.3. *Boundary conditions for the Orr–Sommerfeld equation*

The Orr–Sommerfeld equation (8) is a fourth-order ordinary differential equation and hence requires four boundary conditions. Two boundary conditions are applicable at the mean flow–wall interface at $x_3 = z_0$. These are obtained from the first two rows of (25) by setting the left-hand sides of the two rows to zero; that is

$\hat{\eta}_1(z_n) = \hat{\eta}_3(z_n) = 0$, representing the condition that the last compliant layer is firmly bonded onto a rigid base. These boundary conditions, which are functions of α and ω, cannot be given a simple explicit form; they are implemented within the scheme of numerical solution.

Admissible disturbance modes $\phi(x_3)$ are assumed to decay to zero as x_3 tends to infinity. This yields the following boundary conditions on ϕ:

$$\begin{bmatrix} \alpha\chi & \alpha+\chi & 1 & 0 \\ 0 & \alpha\chi & \alpha+\chi & 1 \end{bmatrix} \boldsymbol{\phi} = \boldsymbol{0} \quad \text{at large } x_3, \tag{26}$$

where $$\chi = (\alpha^2 + \mathrm{i}\alpha R_\delta(1-c))^{\frac{1}{2}}, \quad \mathrm{Re}\,(\chi) > 0 \quad \text{and} \quad \mathrm{Re}\,(\alpha) > 0.$$

In practice the boundary conditions (26) are applied somewhere in the free stream. A value of $x_3 = 6$ (displacement thicknesses), which is about twice the boundary-layer thickness, is used for the results reported in this paper.

With the boundary conditions (26) and the two boundary conditions obtained from (25) by setting $\hat{\eta}_1(z_n) = \hat{\eta}_3(z_n) = 0$, the stability eigenvalue problem involving the OS equation is now complete. We denote the eigenvalue relation symbolically by

$$\mathscr{F}(\alpha, \omega, R_\delta) = 0.$$

The solution of the eigenvalue problem may be achieved by some of the standard procedures described in Drazin & Reid (1981). The compound matrix method of Ng and Reid (1979) is used for integrating the OS equation. The implementation details are given in Yeo (1986).

The above theory is quite general and is applicable to layered anisotropic compliant walls whose materials exhibit material-property symmetry about the (x_1, x_3)-plane. If the symmetry condition is not satisfied, x_1-propagating wave modes within the wall layers will be three-dimensional. The flow disturbance velocity component u_2 will then be coupled to the components u_1 and u_3 via the three-dimensional dynamics of the compliant wall. The resultant stability problem will then be three-dimensional. The symmetry ensures that two-dimensional wall modes compatible with the OS flow modes exist.

2.3. *Specification of properties*

We next consider the detailed specifications of properties for the transversely isotropic materials studied in this paper. From §2.1.2 we note that the mechanical properties of a homogeneous transversely isotropic material are determined when the five parameters G, G', ν, ν' and E' are specified. This represents a dramatic reduction from the maximum of 21 moduli for the most general anisotropic material and 13 for the most general anisotropic material possessing a single plane of symmetry. But it is still a significant increase in number from the two (possibly complex) parameters required to specify an isotropic material. Furthermore, there is also the geometric parameter A_f. Thus six parameters (excluding layer thickness) must be specified for each transversely isotropic layer instead of just two for an isotropic layer. This represents a formidable variety considering that some of the parameters may be complex when there is internal damping. For the sake of simplicity and to keep the study manageable, we would prefer to have as few parameters as possible that need specifying. Some limitations would hence have to be placed on the range of transversely isotropic materials under study. The restrictions must, however, allow adequate scope for the kind of anisotropic responses we wish to study.

To limit the range as much as possible and also retain the directional characteristics of the material and hence of the wall, we set $G = G'$ and $\nu = \nu'$. This makes the

material behave quite isotropically in shear and reduces the number of independent parameters to three; namely G, ν and E'. When E' is given the value of $2G(1+\nu)$ we have an isotropic material.

Next we consider the introduction of viscous damping. Since the materials of interest are behaviourally quite close to isotropic materials, we shall adapt available damping models for isotropic material to our case. For an isotropic medium which is Voigt-deviatoric (Voigt-damped shear mode) and elastic-dilatational (elastic bulk mode), the shear modulus G and Poisson's ratio ν have form

$$G = \rho C_t^2 - i\omega d, \quad \nu = (3K-2G)/2(3K+G), \tag{27a, b}$$

where ρ is the density, C_t the elastic shear speed, d the damping coefficient and K (real) the elastic bulk modulus of the material (see Bland 1960). C_t is the speed of shear wave in the absence of damping ($d = 0$). G and ν are therefore specified functions of frequency ω when ρ, C_t, d and K are given. The properties of the isotropic-material compliant walls studied in I were specified in this manner.

We can extend the above to the restricted class of transversely isotropic materials studied here by assuming their G and ν values to be similarly given by (27). This amounts to saying that the material behaves like a damped isotropic material in shear. In the special context of fibre-reinforced materials, it can be interpreted in an intuitive sense to specify the properties of the isotropic matrix. It is also reasonable to incorporate some damping into the Young's modulus E'. This is because uniaxial extension and compression of say a fibre-reinforced material along the axis of isotropy (fibre axis) will also stretch and compress the damped matrix. Rather than introducing an additional damping coefficient, however, E' is allowed to take on an amount of damping equal to that of the imaginary part of $E = 2G(1+\nu)$; that is, the amount of damping it would have if the material were to be isotropic. E' is hence given the form of

$$E' = E_f + i\,\mathrm{Im}\,(E). \tag{28}$$

E_f, the real part of E', is the elastic Young's modulus of the material along the fibre axis. When E_f is large, extension and compression of the material along the fibre axis is strongly resisted. We also note that when $K \gg |G|$, $\nu_i \ll \nu_r$. A value of $E_f = 3\rho C_t^2$ then closely approximates the case for damped isotropic materials. When the damping coefficient $d = 0$, the parameters G, ν and E' are all real and the material is elastic.

To summarize, the properties of the transversely isotropic materials studied here are specified by the five parameters ρ, C_t, d, K, E_f and the geometric parameter A_f. This is two more than are required for each isotropic layer. E_f determines the *strength* of the anisotropy and can be varied from the near-isotropic value of $3\rho C_t^2$ to a large value for the case of highly inextensible fibres. A_f sets the *orientation* of the anisotropy with respect to the (x_1, x_2, x_3) frame. From these, the G, ν and E' are determined via (27) and (28). The moduli tensor for the stability problem $[C_{pqrs}]$ is then obtained using (5) and (6).

The physical parameters of the compliant wall layers are non-dimensionalized as in §2.2.2 so that

$$\rho = \frac{\rho^{(d)}}{\rho_f^{(d)}}, \quad C_t = \frac{C_t^{(d)}}{U_\infty^{(d)}}, \quad d = \frac{d^{(d)}}{\rho_f^{(d)} U_\infty^{(d)} L_w^{(d)}}, \quad K = \frac{K^{(d)}}{\rho_f^{(d)} [U_\infty^{(d)}]^2}, \quad h = \frac{h^{(d)}}{L_w^{(d)}}. \tag{29a–e}$$

The material density ρ is assumed to be 1.0 for all the cases studied in this paper. The wall lengthscale $L_w^{(d)}$ is defined implicitly by specifying the reference Reynolds number $R_w = 2 \times 10^4$ throughout.

2.4. *Basic wave characteristics*

Wave propagation in transversely isotropic materials is necessarily more complex than that for isotropic media. Whereas the fundamental plane waves in an isotropic medium are either purely longitudinal (displacement of particles in the direction of wave propagation – bulk waves) or purely transverse (displacement perpendicular to the direction of propagation – shear waves), they are seldom purely longitudinal nor purely transverse for an anisotropic medium except along certain principal directions related to the anisotropy. Applying (12) in the material-property frame, a two-dimensional plane wave propagating in the $(x_1^{(m)}, x_3^{(m)})$-plane along the fibre axis $x_3^{(m)}$ with the wavenumber vector $(0, 0, \gamma^{(m)})$ satisfies the equations

$$(C_{1313}^{(m)}[\gamma^{(m)}]^2 - \rho\omega^2) B_1 = 0, \tag{30a}$$

$$(C_{3333}^{(m)}[\gamma^{(m)}]^2 - \rho\omega^2) B_3 = 0, \tag{30b}$$

since $C_{1113}^{(m)} = C_{3313}^{(m)} = 0$ according to (5). The equation corresponding to B_2 is ignored above for reasons given in §2.2.2. Using (5), the determinantal equation of (30) yields the following wave speeds $\mathrm{Re}\,(\omega/\gamma^{(m)})$:

$$c_1^{(m)} = \mathrm{Re}\left[\frac{G'}{\rho}\right]^{\frac{1}{2}}, \quad c_2^{(m)} = \mathrm{Re}\left[\frac{E' + 4(\nu')^2 M^{-1}}{\rho}\right]^{\frac{1}{2}}. \tag{31a, b}$$

Since $G = G'$, it is noted from (27*a*) that $c_1^{(m)} = C_t$ when $d = 0$. $c_2^{(m)}$ is greater than $c_1^{(m)}$. The successive substitutions of $c_1^{(m)}$ and $c_2^{(m)}$ into (30) show that they correspond respectively to the propagation of purely transverse and purely longitudinal waves in the $x_3^{(m)}$-direction. In the same manner it can be shown that purely transverse and purely longitudinal fundamental plane waves, having wave speeds of $\mathrm{Re}\,(G'/\rho)^{\frac{1}{2}}$ and $\mathrm{Re}\,((G + M^{-1})/\rho)^{\frac{1}{2}}$ respectively, may propagate along the $x_1^{(m)}$-axis. Except for these principal directions, the fundamental plane waves propagating in the $(x_1^{(m)}, x_3^{(m)})$-plane are neither purely transverse nor purely longitudinal. In the absence of material damping, the wave speeds in the other directions are bounded above by $c_2^{(m)}$ and below by $c_1^{(m)} = C_t$.

The above concerns wave propagation within the material. When there is a boundary to the material, surface waves propagating along the boundary can also appear. Free-surface waves are the surface waves that can exist in the absence of any traction at the boundary. The free-surface wave modes of the compliant layer can also be determined from the theory of §2.2.2. Since $\hat{\eta}_1(z_n) = \hat{\eta}_3(z_n) = 0$ for compliant layers bonded onto a rigid base, we have from (21)

$$[\hat{\sigma}_{31}, \hat{\sigma}_{33}]_{z_0}^{\mathrm{T}} = \boldsymbol{Z}\,[\hat{\eta}_1, \hat{\eta}_3]_{z_0}^{\mathrm{T}}, \tag{32}$$

where

$$\boldsymbol{Z} = -\begin{bmatrix} P_{13}^{\mathrm{O}} & P_{14}^{\mathrm{O}} \\ P_{23}^{\mathrm{O}} & P_{24}^{\mathrm{O}} \end{bmatrix}^{-1} \begin{bmatrix} P_{11}^{\mathrm{O}} & P_{12}^{\mathrm{O}} \\ P_{21}^{\mathrm{O}} & P_{22}^{\mathrm{O}} \end{bmatrix}.$$

P_{ij}^{O} is the (i,j)-component of the overall propagation matrix $\boldsymbol{P}^{\mathrm{O}}$. In the case of free-surface waves, there is zero traction at the top surface; $\hat{\sigma}_{33}(z_0) = \hat{\sigma}_{31}(z_0) = 0$. Non-trivial wave modes then exist provided

$$\mathrm{Det}\,\boldsymbol{Z} = 0. \tag{33}$$

Equation (33) is the eigenvalue relation which relates the wave (phase) speed c and the wavenumber α for free-surface waves on a layered compliant wall. Material damping is assumed to be absent when computing the free-surface wave modes.

The eigenvalue relation (33) is highly complex even for an isotropic layer. For any given wavenumber α, there is usually an infinite spectrum of wave speeds c.

C_t	E_t	$\lvert A_t\rvert$	c_R
0.7	1.47*	60°	0.6687
	4.0		0.7471
	9.5		0.7661
	20.0		0.7726
	75.0		0.7773
	1200.0		0.7800
0.7	4.0	75°	0.7039
		60°	0.7471
		45°	0.7970
		30°	0.7579
0.5	0.75*	45°	0.4776
	5.0		0.6067
	10.0		0.6197
	14.0		0.6234

* Indicates isotropic case.

TABLE 1. Values of c_R for transversely isotropic single-layer walls with $\rho = 1.0$, $d = 0$ and $K = 500.0$.

Determination of wave speeds is normally accomplished by numerical search procedures. From the viewpoint of the stability study, only the lowest free-surface wave speed c_R is of some interest. It corresponds intuitively to the 'softest' dynamic mode of the compliant wall, and this mode is therefore likely to be the first to become 'sensitive' to the disturbances present in the flow. Indeed, the inviscid work of Yeo & Dowling (1987) and viscous work of Yeo (1986) show that significant interactions between the compliant wall and flow disturbances, both of the desirable and undesirable kinds, take place only when the c_R is somewhat less than the free-stream velocity U_∞ of the flow.

Because of the close relationship of the present type of anisotropy to isotropic material, the free-wave spectra of the transversely isotropic single-layer walls studied here bear qualitative similarities with the spectra of isotropic single-layer walls. In general, the wave speeds c increase in value as α becomes smaller. As α becomes large, the branches of the c-eigenvalue decrease in value and tend rapidly to finite limits. c_R is therefore frequently given by the lowest c-eigenvalue at infinitely large α; and its value is independent of layer thickness h. For isotropic-material layers c_R is just the speed of the well-known Rayleigh surface wave. In the case of multi-layer compliant walls, c_R may belong to a mode with finite α, and can only be determined after a thorough eigenvalue search.

The values of c_R for some of the anisotropic walls examined in this paper are given in table 1. The values of c_R are independent of the sign of the angle A_t and are hence given in table 1 for absolute values of A_t. c_R is normally larger than the corresponding isotropic value when $E_t > 3\rho C_t^2$. For a given A_t, c_R tends to a finite limit as E_t becomes very large. For a given E_t, c_R frequently attains its maximum value for an $|A_t|$ between 40° and 50°, and minimum value at $|A_t| = 0$ or 90°.

3. Results and discussion

Flows over compliant surfaces are susceptible to a wide variety of instabilities. At the broadest level, an instability is either a Tollmien–Schlichting instability (TSI) or a compliance-induced flow instability (CIFI). The former denotes instabilities that

are a modified form of the instability that originally exists on a rigid wall. Fluid viscosity is essential to their existence. The second category covers all instabilities which are brought into being by the compliant response of the wall. These are effectively suppressed when the wall becomes sufficiently stiff. Among the CIFI, three main types may be identified. The first two of these are related to the surface-wave modes and the static deformation modes of the compliant wall; see Yeo & Dowling (1987). They are termed the travelling-wave flutter and the static-divergence (abbreviated SD) instabilities respectively. The third type of CIFI is akin to the classical Kelvin–Helmholtz instabilities and occurs when the wall or the surface is so soft that there is no real phase speed c_r at which it can resist the pressure fluctuations of the flow.

The instabilities may alternatively be classified as Class A, B or C in accordance with the 'activation'-energy scheme proposed by Benjamin (1963). The Tollmien–Schlichting (TS) and the SD modes are Class A instabilities. These modes are initiated by the extraction of energy from the coupled system and are therefore destabilized by wall damping. The flutter modes are Class B. They require positive activation energy and are stabilized by wall damping. Class C modes require little or no activation energy and a prime example is the Kelvin–Helmholtz instability.

We are interested in the stability of the Blasius boundary layer over compliant walls which have material densities which are equal to that of the flow. Results concerning the effects of the anisotropy parameters A_f and E_f on the TSI and the flutter instability modes are described in §§3.1–3.4. Section 3.3 compares cases with opposite fibre orientation whilst in §3.4 a class of two-layer walls bearing some similarity with the walls of Grosskreutz and the anisotropic wall model of Carpenter & Morris is examined. Both TSI and flutter instabilities are primarily convective instabilities; spatial modes (having real frequency ω and complex wavenumber $\alpha = \alpha_r + i\alpha_i$) are accordingly employed for their study. There is instability, which corresponds to a downstream-growing wave, when $\alpha_i < 0$. When convective instabilities are the primary modes of instabilities, the potential of the wall for delaying transition can be assessed using the empirical e^n-rule of Smith & Gamberoni (1956). According to this rule, a disturbance introduced at an upstream location triggers transition to turbulence when its amplitude grows by a factor of e^n. A value of $n = 8.3$ is used here. The growth factor between two points s_0 and s is calculated according to the formula

$$\frac{|A(s)|}{|A(s_0)|} = \exp\left\{-\frac{2}{m^2}\int_{R_\delta(s_0)}^{R_\delta(s)} \alpha_i \, dR_\delta\right\}, \tag{34}$$

where $|A|$ is a suitably defined disturbance amplitude. s_0 is normally selected to correspond to points on the lower neutral branch. Integrated spatial growth factors according to (34) are computed for fixed values of the non-dimensional frequency parameter $F = \omega/R_\delta$.

The results given in §§3.1–3.4 do not take into account the possible existence of divergence instability. SD instabilities have their origin in the static deformation modes of the compliant walls. Very little is known of the occurrence of SD instability in laminar boundary layers over compliant walls, both theoretically and experimentally. SD instability is usually associated with very soft surfaces. Issues relating to SD instability are examined in §3.5. Here some of the walls which show in §§3.1–3.4 potential for significant transition delay are examined for their susceptibility to SD instability. Finally in §§3.6 and 3.7, we look at the eigenfunctions

and examine the relationship between anisotropic surface response and gain in stability.

In presenting the results below, we adhere to the scheme adopted in I. The instabilities are identified as being either a TSI or a CIFI. In addition, the instabilities are labelled in accordance with Benjamin's energy scheme as either Class A or Class B. For more precise references to the various instability regimes, subscripts are also used.

3.1. *The effects of the anisotropy parameters E_f and A_f (negative values) for anisotropic single-layer walls having $C_t = 0.7$*

Isotropic single-layer walls with elastic shear speed $C_t = 0.7$ were studied in detail in I. It was shown that isotropic single-layer walls with $C_t = 0.7$, while admitting the possibility for strong CIFI, possess considerable potential for delaying transition if the walls are suitably damped. They hence provide a good starting point for our investigation into the effects of the anisotropy. Note that only cases with $A_f < 0$ are considered in this and the next sections. Comparisons with cases having $A_f > 0$ are made in §3.3.

Figure 3 illustrates the effects of E_f on the CIFI and the TSI for a layer with $C_t = 0.7$, thickness $h = 5.0$ and material damping coefficient $d = 0.0049$. The fibre angle A_f is $-60°$ and the isotropic case is well approximated by a value of $E_f = 1.47$. The c_R values for the walls (see table 1) are all less than U_∞, a condition necessary for significant interaction between the wall and the flow to occur. The isotropic case has a TSI regime (figure 3*b*) which is much smaller than the corresponding regime of a rigid wall. However, at this low level of material damping, the isotropic case (figure 3*a*) suffers from strong Class B CIFI. Increase in E_f can be seen in figure 3(*a*) to suppress the CIFI regimes and in figure 3(*b*) to destabilize the TSI regimes.

Increasing E_f from the isotropic value of 1.47 to 4.0 causes the CIFI to split into the B_1 and B_2 regimes. In general the B_2 regimes have very small amplification rates and do not feature importantly in our analyses. At $E_f = 4.0$, the spatial amplification rates of the B_1 regime (at $R_\delta = 4000$, $\alpha_i \approx -0.001$, -0.0025 and -0.0036 at $\omega = 0.2$, 0.3 and 0.4 respectively) are comparable with those of the TSI regime for $E_f = 5.0$ shown in figure 3(*b*). Although the B_2 regime stretches to quite a large R_δ, the maximum growth rate for the B_2 regime is an order lower at $\alpha_i \approx -0.0004$. Further small increases in E_f quickly suppress the B_1 regime; at $E_f = 9.5$, the critical Reynolds number R_δ^{cr} for the B_1 regime is greater than 3900.

Increase in E_f destabilizes the TSI, resulting both in a reduction of the critical Reynolds number R_δ^{cr} and an increase in the unstable ω-bandwidth. Compared to the CIFI, which are largely suppressed with a value of $E_f = 10$, the TSI regimes appear to be much less sensitive to increase in E_f. At $E_f = 20$ and 75, the neutral boundaries of the TSI regimes do not deviate much from that of the isotropic case and they possess unstable ω-bandwidths which are substantially smaller than that of a rigid wall. For the TSI regimes, a larger ω-bandwidth generally indicates a larger maximum amplification rate, as well as an extended R_δ-range of amplification at a given value of the non-dimensional frequency F. These regimes therefore have much lower amplification rates than a rigid wall, which can be confirmed by calculation. At $E_f = 20$, for which the CIFI are unimportant, the maximum spatial growth rate at $R_\delta = 4000$ is less than half the rigid-wall maximum of $\alpha_i \approx -0.0125$ at the same R_δ. Calculations based on the TSI regime (since the CIFI are suppressed) show that a maximum amplification factor of $e^{8.3}$ is reached at the streamwise transition

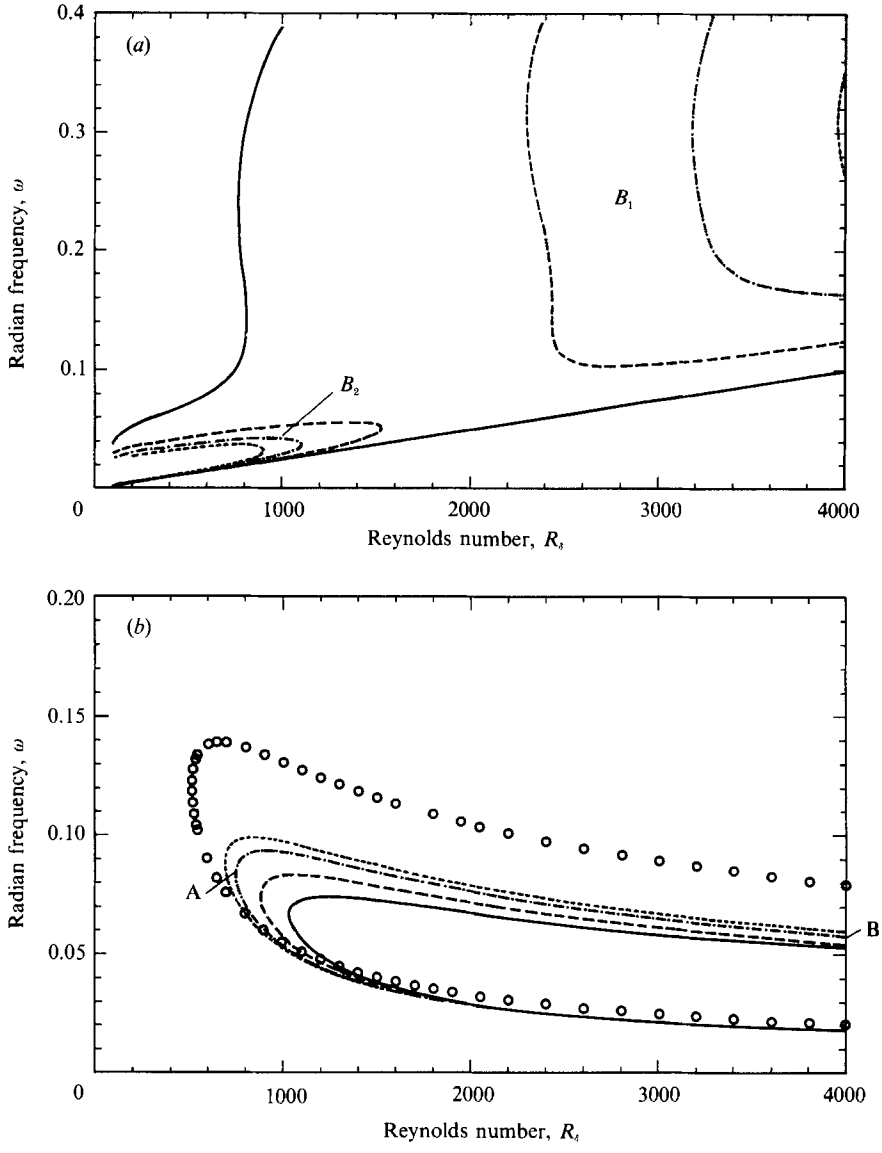

FIGURE 3. The effects of E_f on the marginal stability curves for a layer with $h = 5.0$, $C_t = 0.7$, $d = 0.0049$, $K = 500.0$ and $A_f = -60°$. (*a*) CIFI: ——, isotropic; – – –, $E_f = 4.0$; –·–·–·, $E_f = 6.2$; ·····, $E_f = 9.5$. (*b*) TSI: ——, isotropic; – – –, $E_f = 5.0$; –·–·–·, $E_f = 20.0$; ·····, $E_f = 75.0$; ○, rigid wall.

Reynolds number of $R_x^{tr} \approx 10.97 \times 10^6$ ($R_\delta \approx 5700$). This is 3.86 times the estimated transition distance for a rigid wall which has $R_x^{tr} \approx 2.84 \times 10^6$ ($R_\delta \approx 2900$) for the same factor of growth. The maximum growth factor of $e^{8.3}$ is assumed in the present study to give an approximate criterion for the onset of transition of the flow to a turbulent state. The predicted R_x^{tr} of 10.97×10^6 is close to the value of $R_x^{tr} \approx 11.36 \times 10^6$ given in §4.3 of I for the isotropic case ($E_f \approx 1.47$) in which the dominant CIFI were suppressed by applying a much higher level of material damping. The present results show that the anisotropy provides an effective alternative to material damping as a means to suppress the CIFI to give on balance

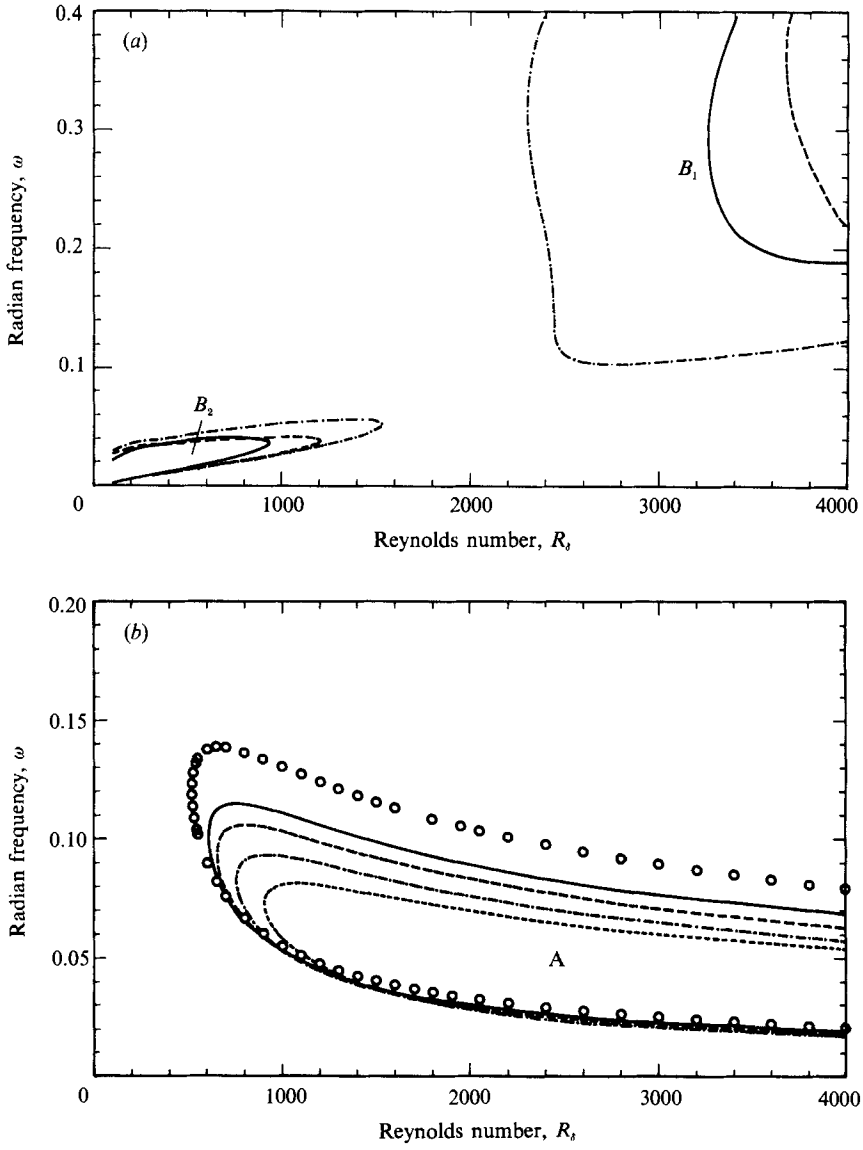

FIGURE 4. The effects of A_f on the marginal stability curves for a layer with $h = 5.0$, $C_t = 0.7$, $d = 0.0049$ and $K = 500.0$. (*a*) CIFI for $E_f = 4.0$. (*b*) TSI for $E_f = 20.0$. ——, $A_f = -30°$; – – – –, $A_f = -45°$; –·–·–·–, $A_f = -60°$; ·····, $A_f = -75°$; ○, rigid wall.

a compliant wall with good potential for delaying transition. The reduction in the critical Reynolds number R_δ^{cr} of the TSI regimes with increase in E_f (figure 3*b*) usually has a small effect on the estimated location of transition.

We next consider the effects of fibre orientation on stability. They are illustrated in figures 4(*a*) and 4(*b*) for CIFI and TSI respectively. The same basic wall with $C_t = 0.7$, $h = 5.0$ and $d = 0.0049$ is used.

Results for the TSI are given for $E_f = 20.0$. Figure 4(*b*) shows that the TSI regime becomes progressively smaller, and therefore less dominant, as $-A_f$ becomes larger. Provided that E_f is larger than the corresponding isotropic value, increasing $-A_f$ whilst keeping E_f constant generally leads to a more stabilized TSI regime; in

particular one with narrower ω-bandwidth in the range of higher R_δ. At smaller values of $-A_f$ (say $< 45°$), TSI regimes are strongly destabilized by even small increases in E_f. To effectively employ the anisotropy to produce significant transition delay, large $-A_f$ appears desirable.

Figure 4(*a*) shows the CIFI regimes at three values of A_f; $-30°$, $-45°$ and $-60°$. A low value of $E_f = 4.0$ is chosen in this case because the CIFI regimes are strongly suppressed at higher values of E_f. The B_2 regimes again possess amplification rates that are much lower than those of the B_1 and the TSI regimes. Only the B_1 regimes are of interest. The B_1 regime appears to be most subdued at $A_f = -45°$. This corresponds to the occurrence of the largest c_R among the three cases (see table 1). As A_f is increased from $-45°$ to larger negative values, the B_1 regime becomes more dominant. This increasing dominance is believed to be related to the falling value of c_R which has its maximum value at $A_f \approx -45°$. c_R can be taken as a qualitative measure of the dynamic stiffness of the wall to short-wavelength instabilities which tend to be associated with flutter instability (B_1), more so than TSI. The smaller c_R is, the 'softer' is the wall and hence the more susceptible it is to flutter instability. In fact, if $-A_f$ is taken to be very large (say $> 80°$), c_R can be very low even for infinitely large E_f. For such large value of $-A_f$, the B_1 regime cannot be suppressed by merely increasing E_f. Other means of suppressing the regime, such as increasing damping, may have to be used.

An optimum combination of A_f and E_f probably exists from the viewpoint of maximum transition delay; one which offers the best balance between the stabilization of the TSI and the B_1 regime. It is, however, computationally expensive to determine this optimum. The effects of the anisotropy remain qualitatively the same at other wall thicknesses. Thicker layers are generally to be preferred because of their lower basic compliance which ensures that the TSI regimes are highly subdued.

3.2. *The effects of E_f and A_f (negative values) for single-layer walls having C_t different from 0.7*

For single-layer isotropic-material walls, results in I indicate that the elastic shear speed C_t, which is related to the elastic shear modulus $(G)_r = \rho C_t^2$, is the most important material parameter determining the compliant quality of the walls. C_t must be somewhat less than 1.0 and greater than 0.5 for significant overall gain in flow stability to be realized.

At $C_t = 1.0$, CIFI are quite unimportant or non-existent. The marginal stability curves of the TSI regimes for isotropic layers with $C_t = 1.0$ (see figure 7 of I) are in general fairly close to that of the rigid wall. Changes in E_f and A_f are found to have small effects on the TSI regimes. Increasing E_f above the isotropic value leads to a stiffening of the wall material and does no more than move the compliant walls' marginal curves progressively closer to the rigid wall's curve.

Figure 5 illustrates the effects of increasing E_f for a layer with $C_t = 0.5$, $h = 5.0$, $d = 0.049$ and $A_f = -45°$. We note that c_R is close to its maximum (for any given E_f) at this value of A_f. The suppressing influence of the anisotropy on the B_1 regime is therefore likely to be quite optimal. For the value of E_f (≈ 0.75) corresponding to an isotropic layer, there exists strong instabilities. The unstable regime marked B_3 (hatched on the unstable side) stretches to near-zero frequency. The unstable regime marked A_B is derived from the coalescence of the TSI and the B_1 regime. Such coalescence occurs in low-C_t walls when the damping is at a high level ($d = 0.049$ for the present case); more examples are given in §4.3 of I. The A_B regime is bounded

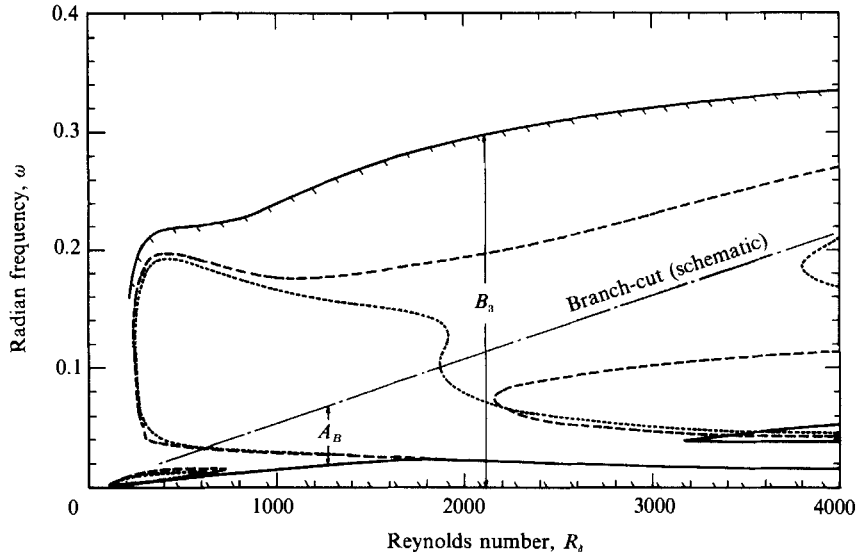

FIGURE 5. The effects of E_f on the marginal stability curves for a layer with $h = 5.0$, $C_t = 0.5$, $d = 0.049$, $K = 500.0$ and $A_f = -45°$. ——, isotropic; – – –, $E_f = 5.0$; · · · · · · · · · · ·, $E_f = 7.0$.

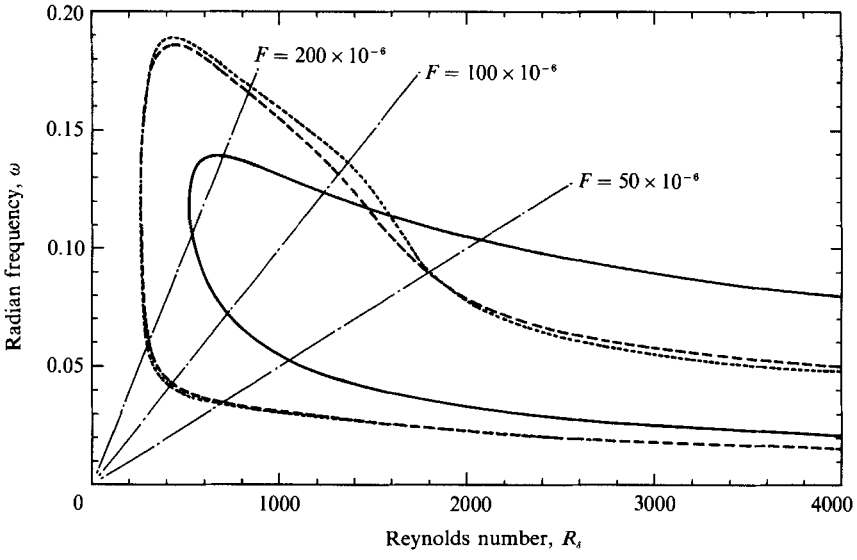

FIGURE 6. The effects of E_f on the marginal stability curves for a layer with $h = 5.0$, $C_t = 0.5$, $d = 0.049$, $K = 500.0$ and $A_f = -45°$. · · · · · · · · · · ·, $E_f = 10.0$; – – – –, $E_f = 14.0$; ——, rigid wall.

above in the (R_δ, ω)-plane by a branch-cut which is indicated schematically. When E_f is increased to 5.0, the B_3 regime is effectively suppressed but coalescence between the TSI and B_1 regimes remains. The coalescence is, however, suppressed at $E_f = 7.0$, with the B_1 regime existing only beyond R_δ of 3800. Thus, at this value of A_f, increase in E_f is seen to be highly effective against the CIFI. Figure 6 shows the TSI regimes for even higher values of $E_f = 10.0$ and 14.0. The CIFI do not appear to be important at these values of E_f. For $E_f = 14.0$, the TSI regime exhibits a very narrow band of unstable frequencies at the higher R_δ, much narrower than that of the rigid

wall's regime. The transitional Reynolds number R_x^{tr} is about 15.3×10^6 ($R_\delta \approx 6720$) for a maximum amplification factor of $e^{8.3}$. Hence, it can be seen that for a soft basic layer ($C_t = 0.5$), the anisotropy still provides an effective way to eliminate the CIFI to give a wall which exhibits considerable potential for delaying transition. The value of A_f is crucial, however. When A_f is increased to $-60°$, the B_1 regime cannot be effectively suppressed for E_f as high as 1200.

3.3. *The case of positive fibre orientation angle*

So far we have only examined cases with negative values of A_f. A typical set of results for walls with oppositely signed values of angle A_f is given in figure 7. The fibre axis points into the oncoming flow when A_f is positive. Figure 7(*a*) shows the marginal stability curves for the B_1 and B_2 regimes for walls with $E_f = 4.0$ and $A_f = -60°$, $+60°$. Again a small value of E_f is chosen for illustrational purpose. The marginal curves for the two walls are almost identical. In the case of TSI regimes, the differences in the stability characteristics of oppositely signed cases are also generally small (figure 7*b*). The differences are only prominent near the *nose* of the regimes, where it may be noted that cases with positive A_f display slightly better stability in the form of a higher critical Reynolds number R_δ^{cr}. A difference of about 200 in the R_δ^{cr} in favour of the case with positive A_f is observed for $E_f = 20.0$. The improved stability is consistent with the expectation that negative Reynolds shear stress τ_R, which is induced by positive A_f, promotes stability. However, these differences between cases with oppositely signed A_f may not be important as far as transition delay is concerned. This is because the potential of the walls for significant transition delay (based on the e^n criterion) is to a large extent determined by the growth rates of the TSI regimes in the range of higher R_δ, say above 2000. At higher R_δ, we can see from figure 7(*b*) that the differences in the marginal curves for oppositely signed cases are really quite small. Calculations confirmed that the spatial growth rates are also nearly identical for the walls. The predicted R_x^{tr} are consequently nearly the same.

The results described above are generally valid for other walls when $|A_f|$ is sufficiently large, $|A_f| > 45°$ say. Cases with smaller $|A_f|$ tend to show somewhat greater differences in their stability characteristics to a change in the sign of A_f. These cases are viewed with less interest here because, as noted before, the TSI regimes are then strongly destabilized by a small increase in E_f above the isotropic value. It is also observed that, in general, the differences in the stability characteristics due to the sign of A_f diminish with increasing R_δ.

3.4. *Two-layer anisotropic walls*

In this section we extend our study to cases of a specific class of two-layer walls which comprise a thin stiff layer of isotropic material bonded onto a much thicker but softer layer of transversely isotropic material. In practice, the employment of a thin stiff outer (top) layer may be necessary to protect the soft underlayer from accidental damage. This practical feature is also manifested in the naturally evolved skin layer of the dolphins according to the study of Kramer (1965). Although the formulation allows multiple anisotropic layers to be treated, the configuration studied has been kept simple to reduce the number of parameters that have to be specified. The two-layer walls investigated have overall thickness $h = 5.0$. The top layer is a thin layer ($h^{(1)} = 0.25$) of a relatively stiff isotropic material with $C_t^{(1)} = 3.0$ and $d^{(1)} = 0.0049$. The bracketed superscript denotes the layer number. The anisotropic second layer is selected to have a low matrix $C_t^{(2)} = 0.5$ and $d^{(2)} = 0.0049$ to secure good stability for

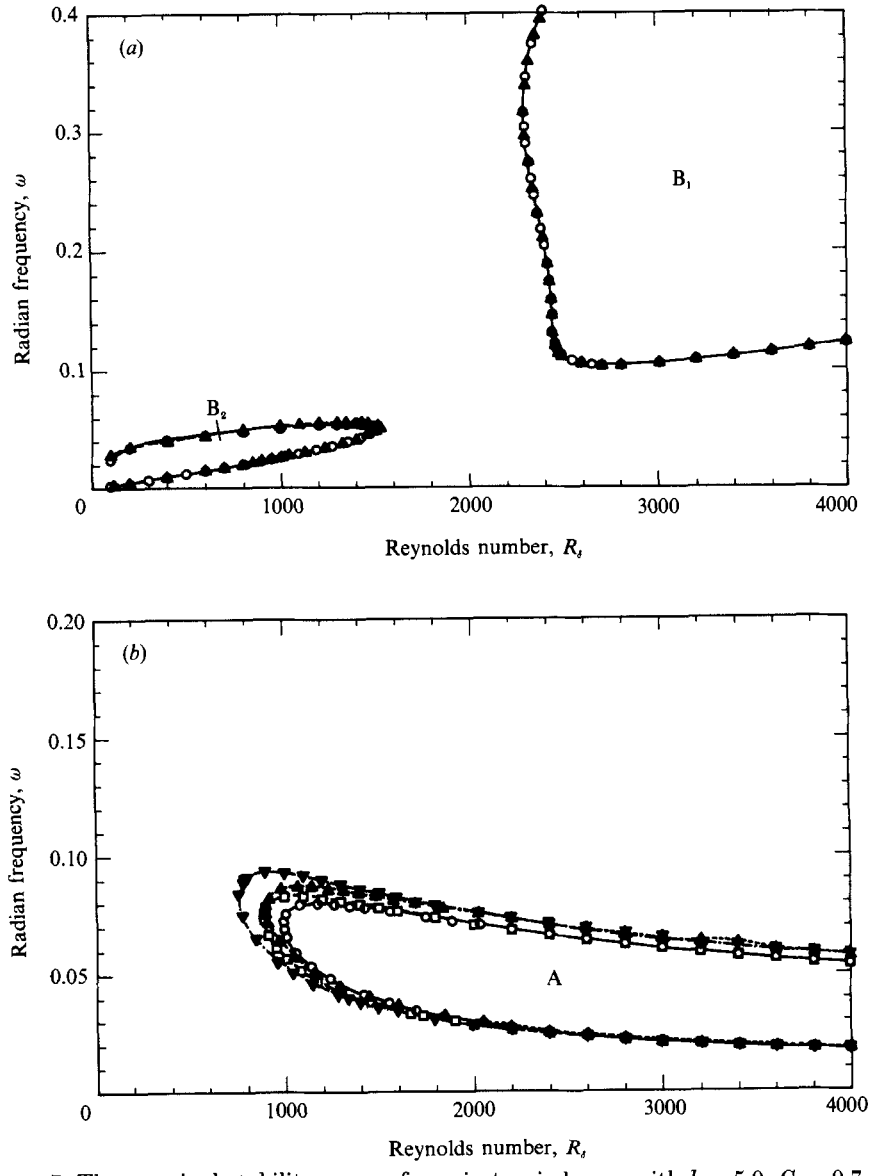

FIGURE 7. The marginal stability curves for anisotropic layers with $h = 5.0$, $C_t = 0.7$, $d = 0.0049$ and $K = 500.0$. Comparison of positive and negative values of A_t. (*a*) CIFI: —○—, $A_t = 60°$, $E_t = 4.0$; --▲--, $A_t = -60°$, $E_t = 4.0$. (*b*) TSI: —○—, $A_t = 60°$, $E_t = 5.0$; --□--, $A_t = -60°$, $E_t = 5.0$; -----▲-----, $A_t = 60°$, $E_t = 20.0$; ·—·▼·—·, $A_t = -60°$, $E_t = 20.0$.

the TSI regime at the larger R_δ. The two-layer walls also bear similarity with Grosskreutz's walls and the plate/sprung-lever model of Carpenter & Morris. When $E_f^{(2)}$ is large, the second layer exerts a strong restraining action on the motion of the top layer along the fibre axis.

In many respects, it is found that the effects of the anisotropy of the second layer on flow stability are qualitatively similar to those already observed for single-layer walls. Below, we shall be contented merely with presenting some cases which demonstrate the potential of such anisotropic two-layer walls for delaying transition.

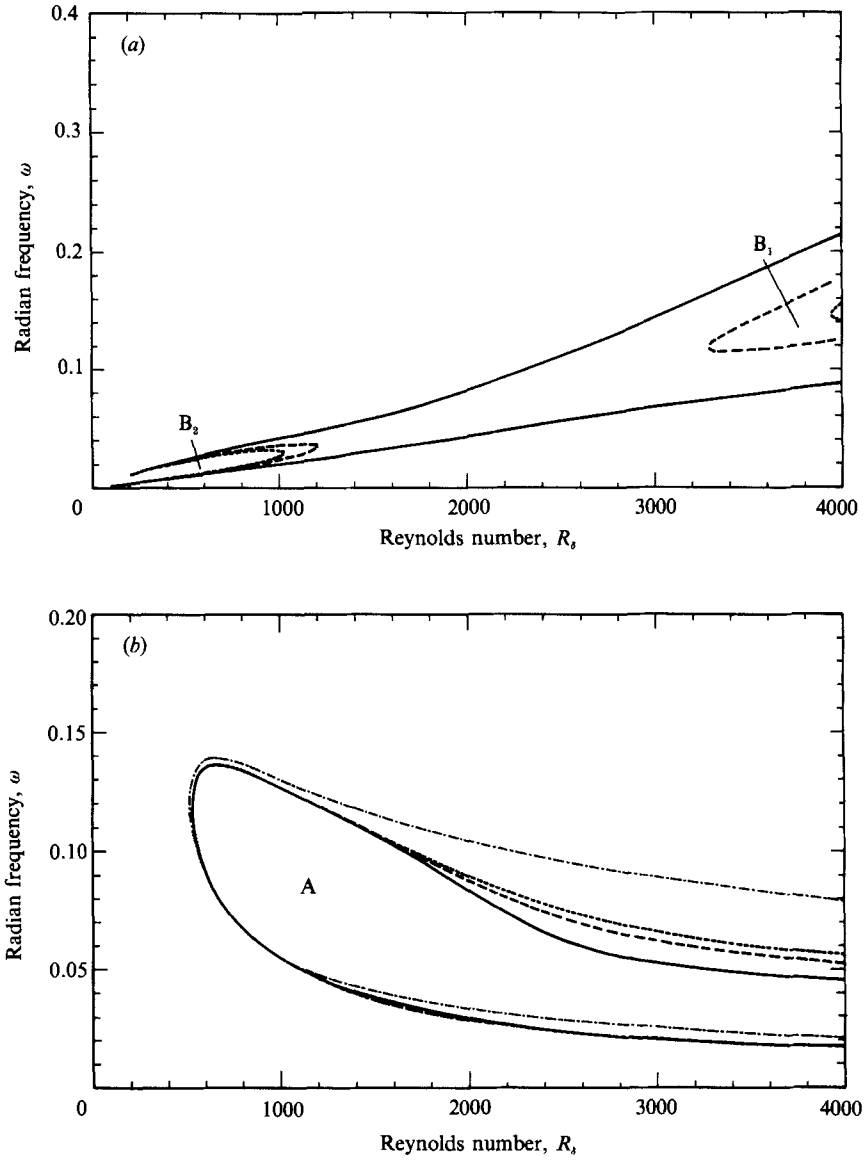

FIGURE 8. The effects of E_f (second layer) on the marginal stability curves for a two-layer wall. Layer 1: $h = 0.25$, $C_t = 3.0$, $d = 0.0049$, $K = 1200.0$, isotropic. Layer 2: $h = 4.75$, $C_t = 0.5$, $d = 0.0049$, $K = 500.0$, $A_f = -60°$. (*a*) CIFI: ——, $E_f^{(2)} = 10.0$; – – – –, $E_f^{(2)} = 20.0$; · · · · · · · · · ·, $E_f^{(2)} = 24.5$. (*b*) TSI: ——, $E_f^{(2)} = 10.0$; – – – –, $E_f^{(2)} = 20.0$; · · · · · · · · · ·, $E_f^{(2)} = 30.0$; – · – · – · –, rigid wall.

Figure 8 shows the effects of increasing $E_f^{(2)}$ on the marginal stability curves for a fibre orientation angle of $A_f^{(2)} = -60°$. Figure 8(*a*) shows the progressive suppression of the CIFI with increase in $E_f^{(2)}$. At $E_f^{(2)} = 10.0$ there is relatively strong CIFI. These modes can be effectively suppressed by increasing $E_f^{(2)}$. At $E_f^{(2)} = 24.5$, the critical Reynolds number R_δ^{cr} of the B_1 regime is greater than 3900. The remaining B_2 regime is very narrow and again has very small amplification rates. The destabilizing influence of increasing $E_f^{(2)}$ on the TSI regime can be seen in figure 8(*b*). At the value of $E_f^{(2)} = 30$ for which the CIFI are of no consequence, the wall shows a greatly

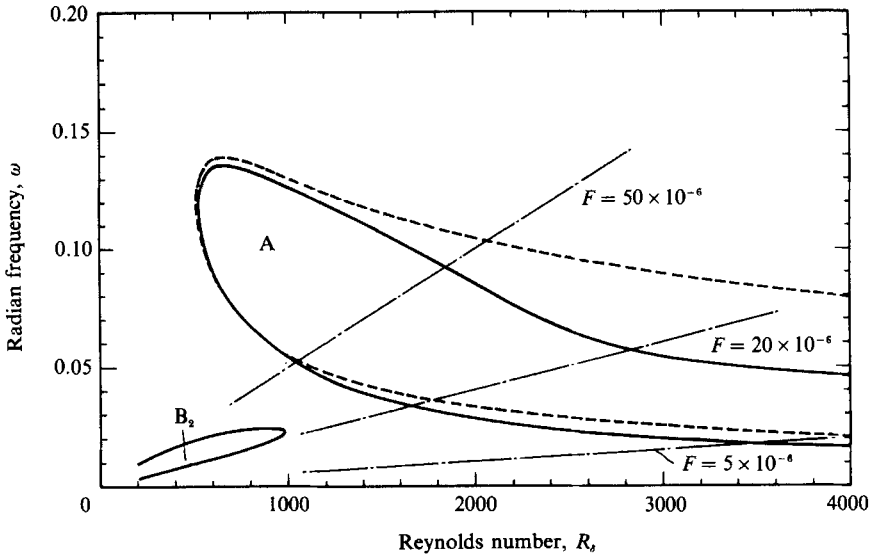

FIGURE 9. The marginal stability curves for a two-layer wall. Layer 1: $h = 0.25$, $C_t = 3.0$, $d = 0.0049$, $K = 1200.0$, isotropic. Layer 2: $h = 4.75$, $C_t = 0.5$, $d = 0.0147$, $K = 500.0$, $A_f = -60°$: $E_f^{(2)} = 10.0$. ——, compliant wall; – – – –, rigid wall.

reduced ω-bandwidth for the TSI regime at large R_δ when compared against the rigid wall's marginal curve. This is highly desirable. At low R_δ, the three marginal curves more or less coincide and are close to the rigid wall's curve. This is mainly the result of the relatively large value of the wavenumber α_w (based on $L_w^{(d)}$) encountered in the *nose* region. The high wavenumber causes the disturbances to be concentrated near the surface of the compliant walls where they are strongly resisted by the relatively high stiffness of the top layer. This can be confirmed by studying the wall eigenfunctions. Such behaviour has also been noted in I for isotropic-material layered walls possessing a stiff top layer.

Another example of a two-layer wall is given in figure 9 for $E_f^{(2)} = 10$ and $A_f^{(2)} = -60°$. Here, instead of increasing $E_f^{(2)}$ to suppress the CIFI as in figure 8, the B_1 regime had been suppressed by increasing the material damping from $d^{(2)} = 0.0049$ to 0.0147. The resulting wall has highly desirable stability characteristics. The ω-bandwidth of the TSI regime at $R_\delta = 4000$ is only very slightly wider than that for $d = 0.0049$ (see figure 8*b* for $E_f^{(2)} = 10$) and is about half that of the rigid wall at the same R_δ. The maximum growth rate at $R_\delta = 4000$ is $\alpha_i \approx -0.003$ compared with a maximum of $\alpha_i \approx -0.0125$ for a rigid wall. The maximum amplification envelope is shown in figure 10 with the envelope of a rigid wall. The maximum growth factor of $e^{8.3}$ is reached at $R_x^{tr} \approx 20.44 \times 10^6$ ($R_\delta \approx 7780$), equivalent to a transition distance 7.2 times that on a rigid wall. Reversal of fibre orientation produces little change in stability. This combination of material damping and anisotropy, both as means to suppress the Class B CIFI, produces a wall that has better stability characteristics than a wall in which the suppression of the CIFI is achieved by either means alone. In the absence of the anisotropy, increase in $d^{(2)}$ alone may result in instability arising from mode coalescence. Increasing $E_f^{(2)}$ alone with $d^{(2)}$ fixed at 0.0049 would lead to significant broadening of the TSI regime at high R_δ (figure 8*b*). This example shows that a suitable combination of damping and anisotropy can be highly desirable. The approach utilizes the fairly well-established fact that an increase in

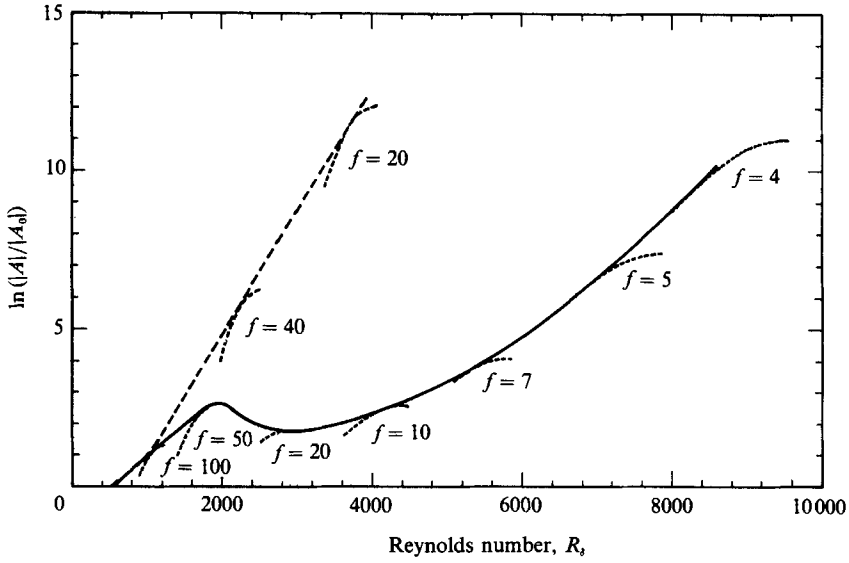

FIGURE 10. The maximum amplification envelopes for the anisotropic two-layer wall of figure 9 and a rigid wall: ——, compliant wall; – – – –, rigid wall. ----------, total amplification curves at $F = f \times 10^{-6}$.

damping has a very small destabilizing effect on the low-frequency TSI modes at high R_δ. The method works provided $E_{\mathrm{f}}^{(2)}$ is sufficiently large that an increase in damping does not lead to coalescence. The estimated transition Reynolds numbers given above and in §§3.1 and 3.2 were not subject to any systematic optimization.

3.5. *Static-divergence instabilities*

The results presented so far pertain mainly to TSI and travelling flutter instabilities. These are primarily convective-type instabilities. The results show that significant reduction in spatial growth rates of TSI modes and effective suppression of convective CIFI can be simultaneously achieved with the appropriate choice of anisotropy parameters. Three examples with transition Reynolds numbers R_x^{tr} much greater than the rigid-wall value of 2.84×10^6 were presented: the single-layer wall of figure 3 with $E_{\mathrm{f}} = 20.0$ ($R_x^{\mathrm{tr}} = 10.97 \times 10^6$); the single-layer wall of figure 6 with $E_{\mathrm{f}} = 14.0$ ($R_x^{\mathrm{tr}} = 15.3 \times 10^6$); and the two-layer wall of figure 9 ($R_x^{\mathrm{tr}} = 20.44 \times 10^6$). These results augur well for the achievement of transition delay provided no other stronger instabilities exist.

An instability of some interest is static divergence (SD). As the name suggests, this is a stationary or very slowly moving instability. SD instability has been observed experimentally by Hansen *et al.* (1980) and Gad-el-Hak, Blackwelder & Riley (1984) on highly damped isotropic viscoelastic layers under turbulent boundary layers. They were detected as two-dimensional surface waves with phase speed typically less than $0.05U_\infty$. The instability waves appeared only when the free-stream velocity U_∞ is much larger than C_{t}, the elastic shear-wave speed of the material; with onset $U_\infty > 3.33C_{\mathrm{t}}$ and $4.5C_{\mathrm{t}}$ respectively according to Hansen *et al.* and Gad-el-Hak *et al.* No SD waves have been observed to date for two-dimensional laminar boundary layers over viscoelastic layers. Gad-el-Hak *et al.* failed to find any SD waves under the Blasius boundary layer for U_∞ as high as $12C_{\mathrm{t}}$. It may be concluded from available experimental results that the onset U_∞/C_{t} ratios for SD instability under

a laminar boundary layer, should it occur, are very high and very much higher than the onset ratios for turbulent layers.

Theoretically, besides the knowledge that SD may be important in very 'soft' walls (low shear modulus – low C_t/U_∞ ratio, low ρ/ρ_f ratio, or both), the conditions for the occurrence of SD in viscous flow is not well known. According to Riley, Gad-el-Hak & Metcalfe (1988) and Carpenter & Morris (1990) SD is an absolute instability; that is to say, an instability which results from the unstable coalescence ($\omega_i > 0$) of an upstream and a downstream eigenstate (Briggs 1964). This is a highly plausible supposition. However, it has proved to be extremely difficult to establish the existence of such SD eigenstates for (viscous) boundary-layer flow if the criteria of Briggs are strictly followed; the author and others have encountered problems with numerical convergence in the vicinity of suspected absolutely unstable SD eigenstates. Temporal eigenmodes (α real and $c = c_r + ic_i$) have customarily been used in the theoretical study of SD instability, identified as unstable eigenstates with small real phase speed c_r.

Duncan, Waxman & Tulin (1985) studied the onset of SD instability on isotropic viscoelastic (Voigt) layers by assuming the pressure fluctuations of the flow to be derived from those of a potential flow modified by a complex scaling factor of the form $K_p \exp(i\theta_p)$. The magnitude scaling factor K_p and the phase shift angle θ_p were obtained from other experimental and theoretical sources. Duncan *et al.* found from extensive computation that SD instability may occur when $U_\infty > 2.86C_t$ in the case of turbulent boundary layers ($K_p = 0.25$, $\theta_p = -10°$). For the turbulent case, their results are in qualitative agreement with the experimental results of Gad-el-Hak *et al.*, both in trends and magnitudes for onset velocity and phase speed. Much higher onset speed $U_\infty > 5.92C_t$ was predicted for laminar boundary layers ($K_p = 0.067$, $\theta_p = -30.4°$). Incidentally, these results can be arrived at more expeditiously by using the theory described in Yeo & Dowling (1987). In fact the theory, suitably modified, shows that SD instability of wavenumber α may only occur for Duncan *et al.*'s pressure model when

$$U_\infty > [E_\alpha^{(n)}/(\alpha K_p \cos\theta_p)]^{\frac{1}{2}}. \tag{35}$$

$\pi E_\alpha^{(n)}/\alpha$ is the elastic energy stored in one x_1-wavelength of the wall due to sinusoidal static deformation of unit amplitude at the surface (precise definition in Yeo & Dowling). For isotropic material layers, $E_\alpha^{(n)}/\alpha$ has a minimum value of $2\rho C_t^2$ at infinitely large α. Using the values of K_p and θ_p assigned by Duncan *et al.*, the criterion (35) indicates that SD instability may occur for turbulent flow when $U_\infty > 2.85C_t$ and for laminar flow when $U_\infty > 5.88C_t$; very close to Duncan *et al.*'s values quoted above.

The occurrence of SD as temporal instabilities in Blasius and turbulent boundary layers over isotropic viscoelastic material layers was studied by Evrensel & Kalnins (1988). The mean turbulent boundary layer is modelled by the $\frac{1}{7}$ power law with linear matching at the wall. They found unstable disturbance modes with $c_r = 0.5$–$0.6U_\infty$ for walls with low to moderate damping. These correspond to the flutter (CIFI) modes of earlier sections. Increasing the damping to a sufficiently high level suppresses these modes but brings into being an instability with c_r just a few percent of U_∞, identified as the SD instability. For turbulent layers, their predictions of onset conditions also show substantially good agreement with the results of Gad-el-Hak *et al.* both in trends and magnitudes (except for wavelength). They also found the onset U_∞ for the Blasius boundary layer to be much higher than those for turbulent layers; the result given has onset $U_\infty \approx 12C_t$.

The maximum U_∞/C_t ratio for the materials of the anisotropic walls studied here, and in particular the three cases which exhibited significant potential for transition delay, is 2.0 (lowest $C_t = 0.5$). This is less than the lowest onset U_∞/C_t ratio quoted in the literature (experimental and theoretical) for turbulent boundary layers, not to mention the much higher ratios expected for laminar layers. For the two-layer case (figure 9), the top layer is of a stiff material with $C_t = 3U_\infty$. It has been found by Chung & Merrill (1984), however, that the attachment of a thin stiff layer over a soft and relatively thick viscoelastic layer strongly inhibits the occurrence of SD waves on the latter. Coupled with the generally low levels of material damping employed (elaborated further on), SD instability appears unlikely to be of importance to the three anisotropic cases.

However, the walls studied here are in general thicker than those reported in the literature, with the exception of Duncan *et al.*'s results which are also applicable to thick layers. Gad-el-Hak *et al.* found that thick layers are more susceptible to SD instability. Their results (figure 6), however, indicate that the onset U_∞/C_t ratio tends to finite limit at large thicknesses. An onset U_∞/C_t limit of 3.5 was given by Hansen & Hunston (1974) for turbulent rotating-disk flow. To be reasonably confident that SD instability is not important for the three anisotropic cases, it was decided to examine their susceptibility in relation to a series of very soft and highly damped isotropic layers. These layers have thickness $h = 5.0$ (equal to that of the three anisotropic cases), $C_t = 0.5$, 0.3 and 0.1 (or $U_\infty/C_t = 2.0$, 3.3, 10.0), and damping coefficient $d = 0.049$. The isotropic layers with $C_t = 0.3$ and 0.1 are clearly much softer and, in quality terms, also much more highly damped (the relaxation time constant $\tau = d/\rho C_t^2$ is a measure of the quality of damping) than the three anisotropic cases. They are therefore expected to be more prone to SD instability than the three anisotropic cases. Figure 11 (*a*) shows the temporal SD eigenstates for these isotropic layers at $R_\delta = 2000$. They correspond to the 'upstream branch' of Duncan *et al.* and the S^- branch of Evrensel & Kalnins. They are all damped modes, with the eigenstates of $C_t = 0.1$ approaching closest to being unstable. Similar damped modes were also found at other R_δ as far as could be ascertained. Since these more compliant and highly damped isotropic cases do not suffer from SD instability, it is considered very unlikely that SD instability will be important for the three anisotropic cases.

For the softest isotropic case, which has $C_t = 0.1$, unstable SD modes with small c_r were, however, found when the damping was increased from $d = 0.049$ to a sufficiently high level. At $d = 0.08$, SD modes was found to exist for R_δ between about 1800 and 2800. A feature of the instability, noted from the calculations, is that it has nearly constant dimensional wavelength $\lambda^{(d)}$ over the range of unstable R_δ. This is because the instability exists within a very narrow wavenumber band, with wavenumber α_w (based on $L_w^{(d)}$) between about 0.071 and 0.076. It has a nearly constant average $\lambda^{(d)}/h^{(d)}$ ratio which is about 16.8 at $R_\delta = 1940$ and 17.2 at $R_\delta = 2760$). For $d = 0.08$, figure 11 (*b*) shows the existence of unstable SD modes of constant $\lambda^{(d)}$ (with $\lambda^{(d)}/h^{(d)} = 17.4$) existing from $R_\delta = 1940$ to 2760. The average phase speed $c_r \approx 0.05U_\infty$. These are in qualitative agreement with the experimental results of Gad-el-Hak *et al.* and their observation that the instability wavelength $\lambda^{(d)}$ does not scale with the local boundary-layer lengthscale. The λ/h ratios obtained here are larger than typical values given in Gad-el-Hak *et al.* for turbulent flow. This could be because the basic flow studied here is laminar and the layers are also significantly thicker than those of Gad-el-Hak *et al.* Furthermore, nonlinear effects are clearly very important in the SD waves observed by them. Further calculations

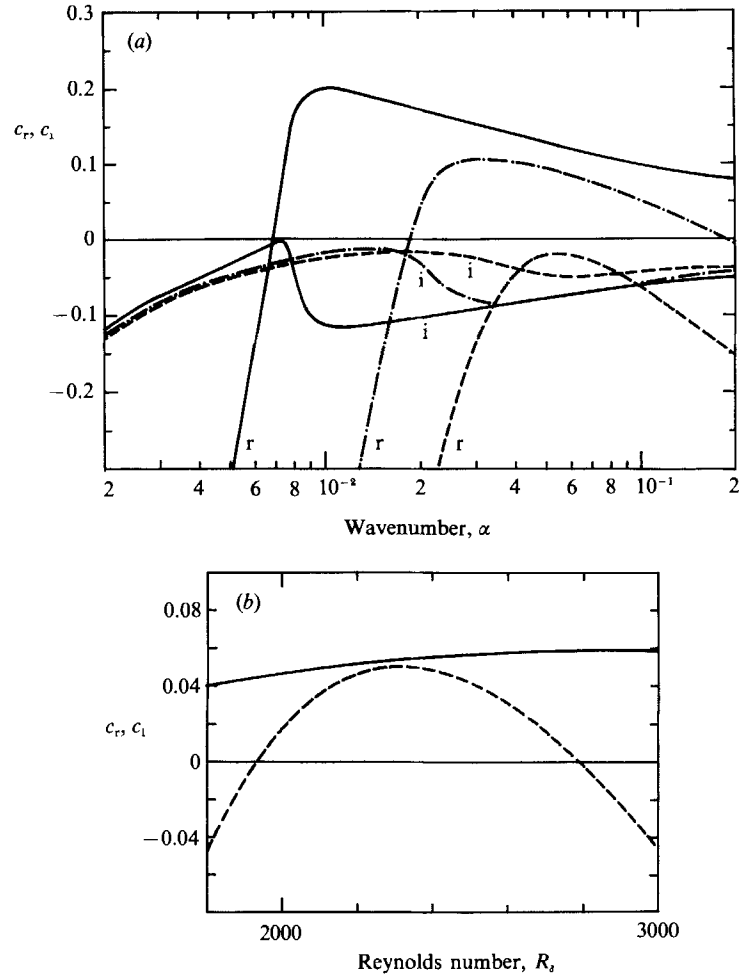

FIGURE 11. (*a*) Temporal SD eigenstates at $R_s = 2000$ for isotropic single-layer walls with $h = 5.0$, $d = 0.049$ and $K = 500.0$: ——, $C_t = 0.1$; ·–·–·–·; $C_t = 0.3$; – – – –, $C_t = 0.5$. r and i denote the real and imaginary parts of c respectively. (*b*) Temporal SD eigenstates for the isotropic single-layer wall with $h = 5.0$, $C_t = 0.1$, $d = 0.08$ and $K = 500.0$. The eigenstates have constant $\lambda^{(d)}$ with $\lambda/h = 17.4$. ——, c_r; – – – –, $10 \times c_i$.

show that the unstable wavelength at the onset of SD instability decreases with reduction in thickness h, much in accordance with what Gad-el-Hak *et al.* observed for turbulent flow.

That SD instability could be brought about by increasing damping when a wall is sufficiently soft suggests that high material damping may be a necessary condition for the existence of SD instability. Similar conclusions may be drawn from the results given by Evrensel & Kalnins. The three anisotropic cases which exhibited potential for delaying transition have rather low damping compared to the walls studied by Gad-el-Hak *et al.* For $U_\infty^{(d)} = 1$ m/s and $\nu_f^{(d)} = 10^{-6}$ m^2 s corresponding to the average conditions of their experiments, the relaxation time constant τ for the most highly damped anisotropic layer studied here (based on $d = 0.049$, $C_t = 0.5$) is about 0.004 s, which is significantly lower than the 1 s quoted by Gad-el-Hak *et al.* for their walls. The isotropic case exhibiting SD instability in figure 11 (*b*) has a relaxation time

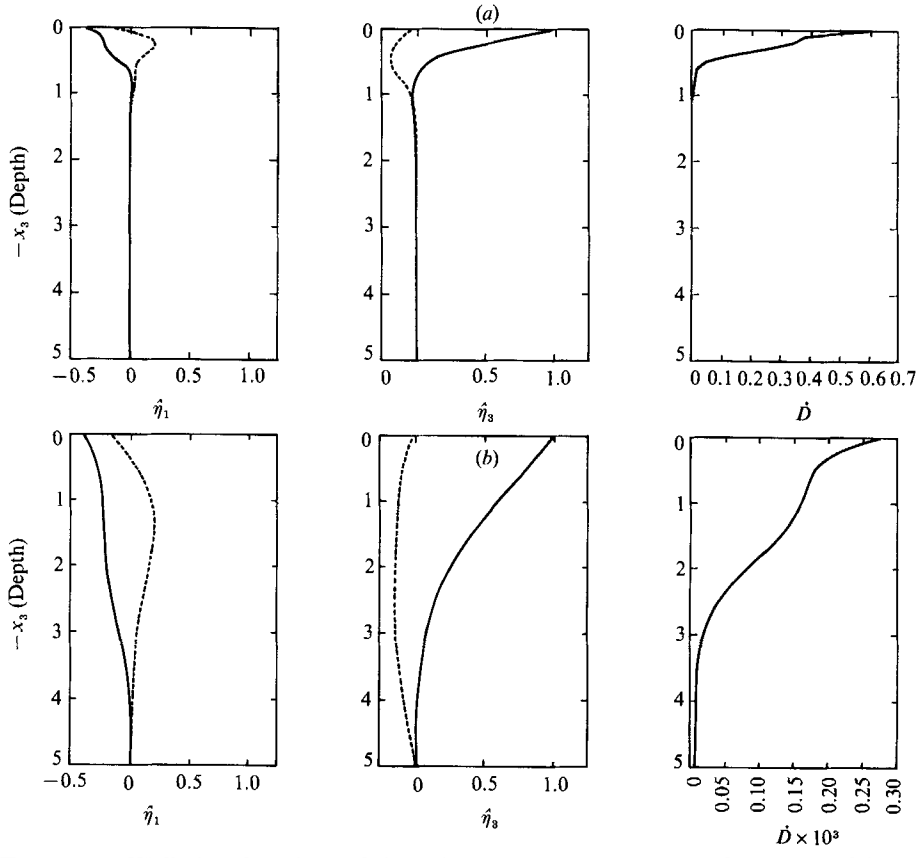

FIGURE 12. Wall eigenfunctions of the anisotropic single-layer compliant wall of figure 3(*b*) having $E_f = 20.0$. (*a*) Eigenstate A. (*b*) Eigenstate B. ——, real part; ----------, imaginary part.

constant of 0.16 s. It is pertinent to note that although the three isotropic cases in figure 11(*a*) with $d = 0.049$ do not appear to suffer from SD instability, they probably suffer from other strong CIFI because of their high compliance.

3.6. *Wall eigenfunctions*

Figure 12 shows the displacement eigenfunctions and the distributions of local dissipation rate for two eigenstates (A and B) of the anisotropic single-layer wall of figure 3(*b*) with $E_f = 20.0$. When E_f is much larger than the corresponding isotropic value, the dominant effect of the anisotropy is the strong restraint it places on wall displacement along the fibre axis. The material particles of the wall then trace out elliptical orbits with their major axes aligned more or less perpendicularly to the fibre axis. The larger E_f is, the narrower are the ellipses, indicating that there is very little displacement along the fibre axis. This results in the significantly large horizontal displacement at the surface that can be seen in figure 12. In contrast, the horizontal displacement at the surface of isotropic-material layers tends to be rather small; see figures 11(*a*, *b*) of I for example. Another distinctive feature of the eigenstates for anisotropic single-layer walls is the tendency for material dissipation to peak at the surface. In the case of isotropic layers, the dissipation at the surface is frequently a minimum point.

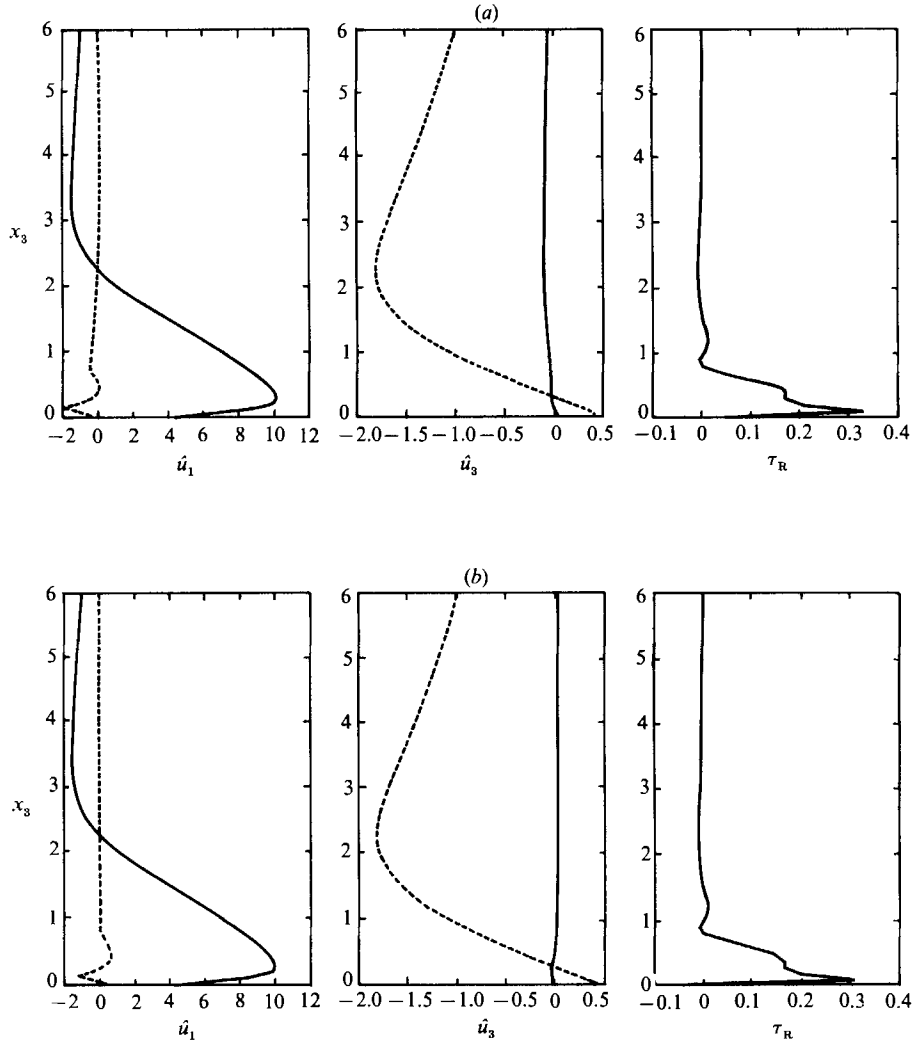

FIGURE 13. Flow eigenfunctions for the eigenstates on the upper neutral branch of the TSI/A regime at $R_\delta = 4000$ for two single-layer compliant walls with $h = 5.0$, $C_t = 0.7$ and $d = 0.0049$. The marginal stability curves are given in figure 7 (*b*). (*a*) $A_f = -60°$, $E_f = 20.0$. (*b*) $A_f = 60°$, $E_f = 20.0$. ——, real part; ----------, imaginary part.

3.7. *On anisotropic response and stability*

Using the non-slip condition (22*a*, *b*), it can be shown that the Reynolds stress τ_R induced at the mean interface ($x_3 = z_0$) as a result of compliant wall motion is given by

$$\tau_R(z_0) = -\overline{(u_1)_r\,(u_3)_r} = -\tfrac{1}{2}\omega^2[\hat{\eta}_3\,\hat{\eta}_1^*]_r\,e^{-2\alpha_i x_1}, \tag{36}$$

where the subscript r denotes the real part. Superscript * denotes complex conjugation. Equation (36) shows that $\tau_R(z_0)$ is derived solely from the correlation between the horizontal (η_1) and the vertical (η_3) components of surface displacement. We note that $[\hat{\eta}_1\,\hat{\eta}_3^*]_r = |\hat{\eta}_1|\,|\hat{\eta}_3|\cos(\hat{\eta}_1, \hat{\eta}_3)$ where $\cos(\hat{\eta}_1, \hat{\eta}_3)$ is the cosine of the angle between $\hat{\eta}_1$ and $\hat{\eta}_3$ in the complex plane. If E_f is sufficiently large, it is easy to see that $[\hat{\eta}_1\,\hat{\eta}_3^*]_r \approx |\hat{\boldsymbol{\eta}}|^2 \sin A_f \cos A_f$. Thus for large E_f, negative (positive) $\tau_R(z_0)$ is generated at

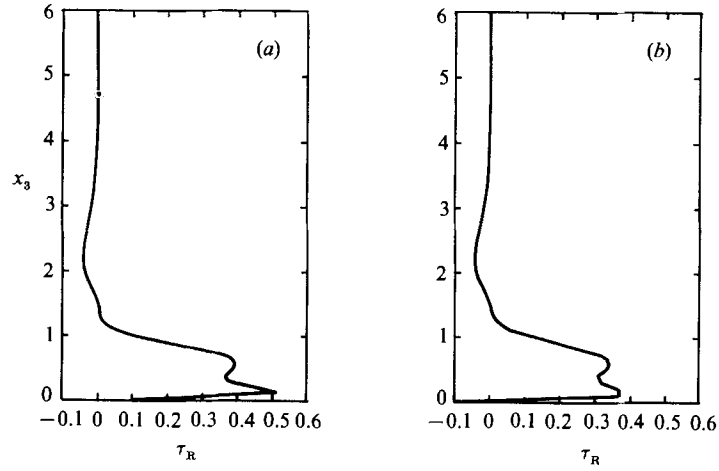

FIGURE 14. Reynolds shear stress (τ_R) distributions for the eigenstates at $R_\delta = 1000$ on the upper neutral branch of the TSI/A regime for the same set of walls as figure 13. (*a*) $A_f = -60°$, $E_f = 20.0$. (*b*) $A_f = 60°$, $E_f = 20.0$.

the wall when A_f is positive (negative). This feature of the anisotropy is amply confirmed by our calculations for both TSI and CIFI modes.

A typical set of results which bear out the above is given in figure 13. The disturbance velocity eigenfunctions and the τ_R distributions belong to the TS eigenstates ($R_\delta = 4000$ on the upper neutral branch) of two anisotropic walls whose neutral curves are given in figure 7(*b*). The walls have $E_f = 20.0$ and are identical except for the opposite orientation of the fibre axis; $A_f = \pm 60°$. As in I, the eigenfunctions are normalized in such a manner that $\sum_{j=1}^{3} \overline{(u_j)_r (u_j)_r}$, termed the mean perturbation kinetic energy, is 1.0 at $x_3 = 6$ (displacement thicknesses) and the Argument of $\hat{u}_{1,3}$ is $-\frac{1}{4}\pi$ at $x_3 = z_0 = 0$. Except for small differences in the vicinity of $x_3 = 0$, where it is noted that τ_R is negative (positive) for $A_f = 60°$ ($-60°$), the two sets of eigenfunctions are very similar. The great similarity between the eigenfunctions underscores the close identity of the two eigenstates and the indifference of the marginal curves in the range of higher R_δ to a change in the sign of A_f, as noted in §3.3. A further set of τ_R distributions for the same set of walls at the lower R_δ of 1000 is given in figure 14. The effect of anisotropic surface response is more evident at this lower R_δ. Positive A_f now favours a noticeably lower level of τ_R over the important region extending from the wall to $x_3 \approx 1$. The beneficial effect of the reduced level of τ_R is reflected in the improved stability that can be seen in figure 7(*b*) ($E_f = 20.0$) near the *nose* for the case with $A_f > 0$. In general, this positive influence (for $A_f > 0$) of the anisotropy on flow stability diminishes with increasing R_δ. In the case of Class B CIFI, their indifference to a change in the sign of A_f, even at fairly small R_δ, is probably a consequence of their highly inviscid nature (inertial origin). In the inviscid limit, the instability is independent of horizontal displacement η_1 and hence of any correlation between η_1 and η_3.

In general, except for fairly small differences in the vicinity of the wall, the flow eigenfunctions of anisotropic and isotropic layers at corresponding eigenstates (same R_δ and approximately equal values of ω and α_i) are very similar. Our eigenfunction results are broadly consistent with those of Domaradzki & Metcalfe (1986) who examined the energetics of small-amplitude Class A and Class B waves over membrane surfaces using a spectral flow-simulation code. For such surfaces, we note that $\eta_1(z_0)$ and hence also $\tau_R(z_0)$ are zero. For the TSI waves, our results show that

much of the activity is concentrated near the wall where the disturbance vorticity has a very strong peak and generally smaller values elsewhere. This is in agreement with Domaradzki & Metcalfe's observation that much of the activity associated with the TSI occurs in a thin layer next to the wall. In spite of this concentration of activity next to the wall, the anisotropic response has surprisingly small effects on the stability, especially at the higher R_δ. Part of the reason may be found in (36) which indicates that, subject to the normalization, the induced $\tau_R(z_0)$, whatever the sign, is proportional to ω^2. The higher-R_δ TSI modes in general have low ω. For the CIFI modes, the eigenfunctions generally show intense activity in the vicinity of the critical layer; and lower levels of activity at the wall, especially at the higher R_δ. This is broadly in agreement with Domaradzki & Metcalfe. The favourable effect of wall damping on the Class B CIFI is then probably communicated to the critical layer primarily via the non-viscous part of the stress field as suggested by them.

It is appropriate at this juncture to mention the recent paper of Carpenter & Morris (1990) on their rigid sprung-lever model. They reported transition Reynolds number R_x^{tr} of similar magnitudes to those presented here. In contrast to the present work, however, their best results were obtained when the levers were inclined at relatively small angles to the vertical, such as $A_f = 15°$ in our notation. From eigenfunction studies, they reasoned that the stabilization of the TSI regimes arose from the favourable long-range influence of their wall anisotropy on the Reynolds stress distribution leading to a significant overall reduction in disturbance energy production. At larger A_f, they found the effects of the anisotropy to be greatly diminished so that the stability characteristics of the walls were quite indifferent to the sign of A_f.

4. Concluding summary

The two-dimensional linear stability of the Blasius boundary layer over transversely isotropic material compliant walls has been studied. The theory formulated is also applicable to other homogeneous-material anisotropy provided that the mechanical properties are symmetrical about the (x_1, x_3)-plane of the stability problem.

For single-layer walls, increase in E_f has been found in general to have a stabilizing effect on the CIFI and a destabilizing effect on the TSI. Examples given show that with the proper choice of anisotropy parameters E_f and A_f, it may be possible to suppress the CIFI with minimal adverse effect on the TSI and hence produce an anisotropic wall with good potential for delaying transition to turbulence. Provided the CIFI (B_1 regime) can be effectively suppressed by increasing E_f, large $|A_f|$ appears to be generally preferable because the destabilizing influence on the TSI is then rather weak. Suitable values of $|A_f|$ are usually greater than or equal to 45°. The choice of E_f and A_f that gives good transition delaying potential also depends rather critically on other parameters of the wall, such as thickness h, shear speed C_t and damping coefficient d. Specific cases of a two-layer anisotropic wall which bear similarity with the Grosskreutz walls and the plate/sprung-lever model of Carpenter & Morris have also been studied. Examples presented show that such walls also possess considerable potential for delaying transition. Transition Reynolds numbers R_x^{tr} of up to 7.2 times the rigid-wall value have been obtained. Calculations indicate that SD instability is unlikely to be important for the anisotropic walls studied.

CIFI eigenstates have generally been found to be quite independent of changes in the sign of A_f. This independence is believed to be a consequence of the highly

inviscid nature of the CIFI. The TSI eigenstates at the larger R_δ have also been found to be independent of the sign of A_Γ. The beneficial effect on flow stability of inducing negative $\tau_R(z_0)$ is only significant at lower Reynolds numbers where an increase in the critical Reynolds number of the TSI regime has normally been observed. At large R_δ, the low frequency of the TSI eigenstates probably contributes to make the induced $\tau_R(z_0)$, whatever its sign, small. Since the TSI regimes at the higher R_δ are largely unaffected by the sign of A_Γ, it is not unreasonable to deduce that the significant gains in stability (and projected transition distances) noted are to a large measure the consequences of some desirable changes to the compliant qualities of the wall, rather than from the direct effect of the anisotropy on the sign of τ_R induced in the vicinity of the wall.

The author wishes to thank Dr Ann P. Dowling for the invaluable guidance and encouragement she has given him during the course of this work. The author also benefitted greatly from the various discussions he had with Professor M. Gaster to whom he would like to register his greatest appreciation herein. The major part of this work was done while the author was on study leave at the University of Cambridge. The financial support of the National University of Singapore and the Commonwealth Trust Fund is gratefully acknowledged.

REFERENCES

BENJAMIN, T. B. 1963 The three-fold classification of unstable disturbances in flexible surfaces bounding inviscid flows. *J. Fluid Mech.* **97**, 436.

BENJAMIN, T. B. 1964 Fluid flow with flexible boundary. In *Proc. 11th Intl Congr. Applied Mechanics, Munich* (ed. H. Görtler), p. 109. Springer.

BLAND, D. R. 1960 *Linear Viscoelasticity*. Pergamon.

BRIGGS, R. J. 1964 *Electron-stream Interaction with Plasmas*. Monograph 29, MIT Press.

CARPENTER, P. W. 1984 The hydrodynamic stability of flows over non-isotropic compliant surfaces. Presented at *European Colloqu. 188, 23–26 Sept. 84, University of Leeds.*

CARPENTER, P. W. 1987 Effect of anisotropic wall compliance on boundary-layer stability. Presented at *European Colloqu. 228, Sept. 87, University of Exeter.*

CARPENTER, P. W. & GARRAD, A. D. 1985 The hydrodynamic stability of flow over Kramer-type compliant surfaces. Part 1. Tollmien–Schlichting instabilities. *J. Fluid Mech.* **155**, 465.

CARPENTER, P. W. & MORRIS, P. J. 1985 The hydrodynamic stability of flows over non-isotropic compliant surfaces – Numerical solution of the differential eigenvalue problem. In *Numerical Methods in Laminar and Turbulent Flows*, p. 1613. Pineridge.

CARPENTER, P. W. & MORRIS, P. J. 1990 The effects of anisotropic wall compliance on boundary-layer stability and transition. Submitted to *J. Fluid Mech.* (in press).

CHUNG, K. H. & MERRILL, E. W. 1984 Drag reduction by compliant surfaces measured on rotating disks. Abstr. submitted to the Compliant Coating Drag Reduction Prog. Rev., Office of Naval Research.

DOMARADZKI, J. A. & METCALFE, R. W. 1986 Stabilization of laminar boundary layers by compliant membranes. *Phys. Fluids* **30**, 695.

DRAZIN, P. G. & REID, W. H. 1981 *Hydrodynamic Stability*. Cambridge University Press.

DUNCAN, J. H., WAXMAN, A. M. & TULIN, M. P. 1985 The dynamics of waves at the interface between a viscoelastic coating and a fluid flow. *J. Fluid Mech.* **158**, 177.

EVRENSEL, C. A. & KALNINS, A. 1988 Response of a compliant slab to viscous incompressible fluid flow. *Trans. ASME* E: *J. Appl. Mech.* **55**, 660.

GAD-EL-HAK, M., BLACKWELDER, R. F. & RILEY, J. J. 1984 On the interaction of compliant coatings with boundary-layer flows. *J. Fluid Mech.* **140**, 257.

GREEN, A. E. & ZERNA, W. 1968 *Theoretical Elasticity*. Clarendon.

GROSSKREUTZ, R. 1971 Wechselwirkungen zwischen turbulenten Grenzschichten und weichen Wänden. *Max-Planck Institut für Strömungsforschung, Göttingen, Mitt.* 53.

GROSSKREUTZ, R. 1975 An attempt to control boundary-layer turbulence with non-isotropic compliant walls. *University Science Journal (Dar es Salaam)* **1**, 67.

HANSEN, R. J. & HUNSTON, D. L. 1974 An experimental study of turbulent flows over compliant surfaces. *J. Sound Vib.* **34**, 297.

HANSEN, R. J., HUNSTON, D. L., NI, C. C. & REISCHMAN, M. M. 1980 An experimental study of flow-generated waves on a flexible surface. *J. Sound Vib.* **68**, 317.

HIRSCH, M. W. & SMALE, S. 1974 *Differential Equations, Dynamical Systems and Linear Algebra.* Academic.

KRAMER, M. O. 1965 Hydrodynamics of dolphins. *Adv. Hydrosci.* **2**, 111.

LANDAU, L. D. & LIFSHITZ, E. M. 1970 *The Theory of Elasticity.* Pergamon.

LEKHNITSKII, S. G. 1963 *Theory of Elasticity of an Anisotropic Elastic Body.* Holden-Day.

NG, B. S. & REID, W. H. 1979 An initial value method for eigenvalue problems using compound matrices. *J. Comput. Phys.* **30**, 125.

RILEY, J. J., GAD-EL-HAK, M. & METCALFE, R. W. 1988 Compliant coatings. *Ann. Rev. Fluid Mech.* **20**, 393.

SMITH, A. M. O. & GAMBERONI, H. 1956 Transition, pressure gradient and stability theory. *Douglas Aircraft Co., Long Beach, CA., Rep.* ES26388.

YEO, K. S. 1986 The stability of flow over flexible surfaces. Ph.D. thesis, University of Cambridge.

YEO, K. S. 1988 The stability of boundary-layer flow over single- and multi-layer viscoelastic walls. *J. Fluid Mech.* **196**, 359 (referred to as I herein).

YEO, K. S. 1990 The three-dimensional stability of boundary-layer flow over compliant walls. *J. Fluid Mech.* (to be submitted).

YEO, K. S. & DOWLING, A. P. 1987 The stability of inviscid flows over passive compliant walls. *J. Fluid Mech.* **183**, 265.